

Measuring Casimir Force Across a Superconducting Transition

Minxing Xu,^{1,2,*} Robbie J. G. Elbertse,^{2,*} Ata Keşkekler,¹
Giuseppe Bimonte,^{3,4} Jinwon Lee,² Sander Otte,^{2,†} and Richard A. Norte^{1,2,‡}

¹*Department of Precision and Microsystems Engineering,
Delft University of Technology, Delft, The Netherlands*

²*Kavli Institute of Nanoscience, Department of Quantum Nanoscience,
Delft University of Technology, Delft, The Netherlands*

³*Dipartimento di Fisica E. Pancini, Università di Napoli Federico II,
Complesso Universitario di Monte S. Angelo, Via Cintia, Napoli, Italy*

⁴*INFN Sezione di Napoli, I-80126 Napoli, Italy*

The Casimir effect and superconductivity are foundational quantum phenomena whose interaction remains an open question in physics. How Casimir forces behave across a superconducting transition remains unresolved, owing to the experimental difficulty of achieving alignment, cryogenic environments, and isolating small changes from competing effects. This question carries implications for electron physics, quantum gravity, and high-temperature superconductivity. Here we demonstrate an on-chip superconducting platform that overcomes these challenges, achieving one of the most parallel Casimir configurations to date. Our microchip-based cavities achieve unprecedented area-to-separation ratio between plates, exceeding previous Casimir experiments by orders of magnitude and generating the strongest Casimir forces yet between compliant surfaces. Scanning tunneling microscopy (STM) is used for the first time to directly detect the resonant motion of a suspended membrane, with subatomic precision in both lateral positioning and displacement. Such precision measurements across a superconducting transition allow for the suppression of all van der Waals, electrostatic, and thermal effects. Preliminary measurements suggest superconductivity-dependent shifts in the Casimir force, motivating further investigation and comparison with theories. By uniting extreme parallelism, nanomechanics, and STM readout, our platform opens a new experimental frontier at the intersection of Casimir physics and superconductivity.

I. INTERPLAY OF CASIMIR FORCES AND SUPERCONDUCTIVITY

The Casimir effect and superconductivity are two landmark quantum phenomena, each showcasing striking macroscopic behavior rooted in quantum mechanics. The Casimir effect [1], predicted by Hendrik Casimir in 1948, arises from vacuum fluctuations of electromagnetic fields and manifests as an attractive force between two closely spaced, uncharged surfaces. In Fig. 1a, we show Casimir's original theoretical setup: two perfectly conducting, parallel plates experience forces that scale as $F \propto A/d^4$, where A is area and d is separation. These extreme geometries amplify quantum fluctuations into measurable macroscopic forces but require precise alignment and sensitive detection to isolate Casimir effects from competing interactions. Although these challenges delayed experimental confirmation for nearly half a century [2], Casimir forces are now known to dominate nanoscale systems as separations shrink.

Superconductivity, discovered in 1911, occurs when electrons form Cooper pairs [3] below a critical temperature (T_C), allowing them to move without electrical resistance (Fig. 1a inset). Above T_C , electrons act as individual particles; below it, they pair into macroscopic quan-

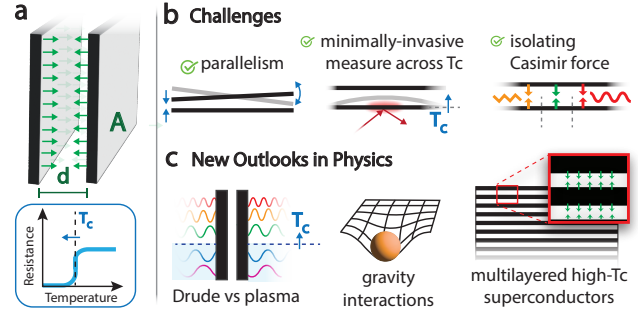


FIG. 1. Superconducting Casimir Force (a) Schematic of a superconducting Casimir cavity, where two plates of area A are separated by a gap d . Inset shows a superconducting transition of the plates. (b) Key challenges in measuring the Casimir effect across T_C , including achieving high parallelism using compliant plates, and ensuring minimally invasive measurement across T_C . Additionally, isolating the Casimir force from electrostatic and measurement-induced contributions remains a significant challenge. (c) The Casimir-superconductivity regime links to long-standing controversy in the low-frequency response optical response of metals (Drude vs. plasma), non-classical gravity, and high- T_C superconductivity in layered cuprates.

tum states with coherence lengths spanning hundreds of nanometers. This sharp transition into the mesoscopic regime makes superconductors one of the most striking phenomena in condensed matter physics.

Although Casimir's original theory assumed perfectly conducting plates, an intriguing question remains: how

* These authors contributed equally to this work.

† a.f.otte@tudelft.nl

‡ r.a.norte@tudelft.nl

do Casimir forces behave when the plates become superconducting? Despite the fundamental importance of both phenomena, their interplay remains experimentally elusive. The sudden onset of superconductivity at T_C offers an opportunity to toggle this interaction on and off, enabling precise differential measurements [4, 5]. Realizing this requires overcoming three primary challenges, outlined in Fig. 1b.

1. Achieving nanometer-scale parallelism at cryogenic temperatures demands exceptional mechanical precision and active feedback control [6, 7], as even slight misalignments distort the Casimir force.
2. Measurements above and below T_C must be minimally invasive (avoiding degradation of the Casimir signal and the superconducting state).
3. Casimir forces must be isolated from competing effects; including thermal expansion, material changes at T_C [8–10], electrostatics [11–13], and artifacts from the measurement itself.

These challenges — exacerbated in cryogenic setups with limited space and complex infrastructure — have kept this regime largely unexplored, leaving the Casimir-superconductivity intersection an open frontier in physics. In this work, we overcome these barriers using a microchip-based platform that achieves ultra-parallel plate configurations and generates record-high Casimir forces. Our platform features free-standing superconducting membranes, whose dynamics across T_C are probed using scanning tunneling microscopy (STM). STM’s atomic-scale precision enables minimally invasive, highly localized readout, allowing systematic suppression of van der Waals, electrostatic, and thermal effects. This provides an exceptionally sensitive detection scheme, offering a first step toward uncovering how superconductivity influences the Casimir force and uniting these two macroscopic quantum phenomena.

The following sections present the theoretical context of Casimir-superconductivity interactions, describe the fabrication of our on-chip cavities, and introduce the STM-based detection method. We then outline protocols for eliminating non-Casimir contributions and report calibrated frequency sweeps across T_C to probe superconductivity-induced shifts in the Casimir force.

II. THEORETICAL IMPLICATIONS AND OPEN QUESTIONS

Understanding how superconductivity influences the Casimir effect could address foundational questions in condensed matter physics, high-temperature superconductivity, and perhaps non-classical gravity (Fig. 1c). The most established framework, the Drude vs. plasma model debate [14, 15], examines how a metal’s optical properties affect Casimir forces. This debate, unresolved for over two decades, centers on whether dissipation via electron scattering (Drude) or dissipationless electron gas (plasma) better predicts metallic Casimir forces. Ob-

serving how the Casimir force changes across T_C could provide valuable insights into resolving this puzzle, with higher T_C enhancing the effects. When a metal transitions to a superconductor, its optical response changes at frequencies on the order of $k_B T_C / \hbar$. However, the Casimir interaction spans much higher frequencies, up to $\omega_c = c/d$ for nanometer-scale separations, suggesting a small impact from superconductivity. Such experiments were attempted twice with no changes in Casimir force across T_C [16, 17] due to insufficient sensitivity to either model [14].

Some speculative theories propose superconductors in Casimir configurations may interact with gravity in ways that depart from classical general relativity [18–22]. While intriguing, these proposals remain unverified and require further theoretical and experimental scrutiny via superconducting Casimir experiments.

Another open question is whether Casimir forces influence T_C . Prior studies detected no shift in T_C within 12 μK for lead (Pb) plates separated by a 70nm gap in a plate-plate configuration[23]. High- T_C superconductors, however, present a unique case. Their layered structures form intrinsic Casimir cavities, where the associated energy may generate internal pressures exceeding 100atm — comparable to their superconducting condensation energies. Recent theories suggest that Casimir interactions in multilayered cuprates may help stabilize high- T_C superconductivity, potentially addressing one of the most enduring and impactful open problems in physics.[24, 25]. Notably, 1960s experiments showed that alternating superconducting and insulating layers enhanced T_C , hinting at a related mechanism [26, 27].

Whether resolving the Drude-plasma debate, probing high- T_C mechanisms, or testing faint gravitational effects, the interplay between superconductivity and Casimir forces offers profound opportunities to advance fundamental physics and materials science with table-top experiments. Yet, experimental challenges have kept this frontier of quantum physics largely unexplored.

III. ULTRA-PARALLEL SUPERCONDUCTING CASIMIR CAVITIES

Over the past decade, a variety of on-chip Casimir geometries have been explored [16, 23, 28–33]. Most conventional setups use a sphere-plate geometry for easier alignment between two surfaces. While plate-plate configurations more closely follow Casimir’s original theory, they require stringent parallelism and mechanical stability, making them rare [6, 7, 23, 29]. To date, no superconducting Casimir experiments have reported measurable force shifts across T_C [16, 17, 23, 34].

Maximizing sensitivity to superconductivity-induced Casimir shifts requires both large Casimir pressures $F_{\text{Cas}} \propto A/d^4$ and high mechanical compliance. Thinner, more flexible membranes respond more sensitively to force variations but are also more prone to stiction

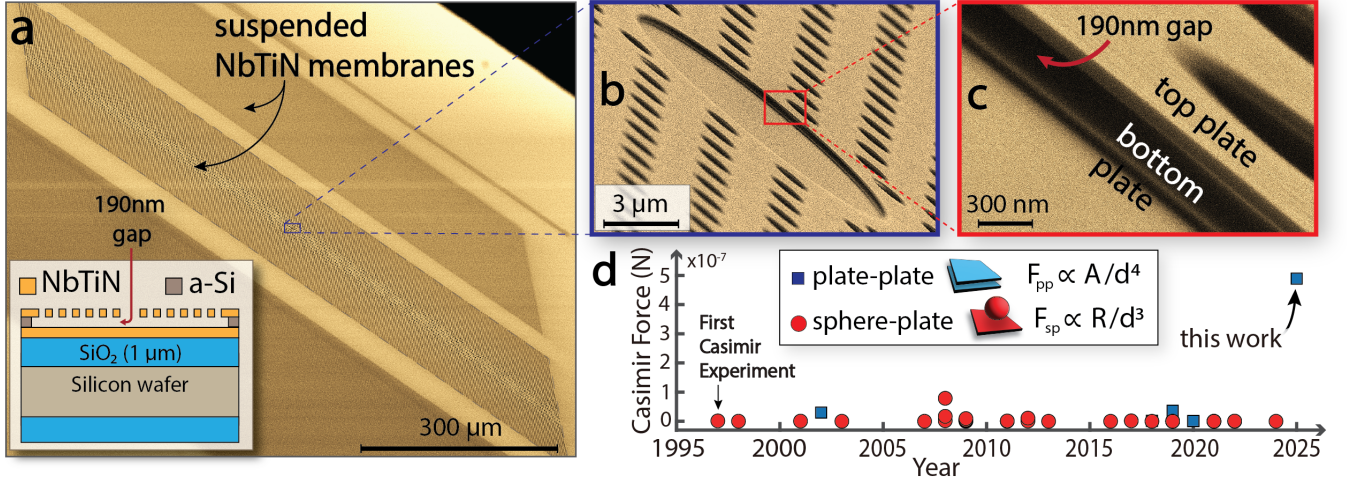


FIG. 2. Achieving extreme parallelism on-chip. (a) Colorized SEM of a microchip with suspended NbTiN (square) membranes above a NbTiN backgate; inset shows the layered structure. Membranes feature micron-scale holes for selective plasma etching of the a-Si layer. A $1\ \mu\text{m}$ SiO_2 layer electrically isolates the Casimir cavity. (b) A central hole in the top membrane offers visual access to the gap. (c) Close-up of 190nm gaps sustained over millimeter-scale areas, with $\sim 130\text{pm}$ sag kept taut by high-stress NbTiN. (d) Comparison of area-over-gap ratios for published Casimir setups. Here, the ideal Casimir force between perfect conductors is used as a consistent metric to quantify effective parallelism. Blue squares: plate-plate ($F \propto A/d^4$); red circles: sphere-plate ($F \propto R/d^3$). Our chip platform’s parallelism surpasses prior cryogenic and room-temperature experiments, achieving the highest Casimir force between compliant surfaces to date. See Supplementary Information J for data sources.

and misalignment, making extreme parallelism harder to maintain. This trade-off defines a key constraint: optimize parallelism for large Casimir forces while maintaining compliance for detectable frequency shifts.

We overcome this trade-off by nanofabricating Casimir cavities directly on silicon chips using high-stress superconducting films. Our monolithic plate-plate design suspends a $709 \times 709\ \mu\text{m}^2$ niobium titanium nitride (NbTiN) membrane above a fixed NbTiN backplate with gaps as small as 190 nm (Fig. 2). High tensile stress ($\approx 680\ \text{MPa}$) keeps the membrane taut and stable, preventing collapse from stiction or adhesion. The cavity is formed by depositing 155 nm-thick NbTiN layers above and below a sacrificial amorphous silicon (a-Si) layer, which is delicately removed via a highly selective SF_6 plasma etch that preserves the NbTiN’s 1–2 nm surface roughness (see Supplementary Information D). After suspension, an adiabatic return to lab conditions from cryogenic vacuum environments prevents collapse, enabling high-yield fabrication. Gap size is tunable by adjusting a-Si thickness. Successfully suspended membranes exhibit fundamental frequencies near 253 kHz in room temperature, confirmed via laser Doppler vibrometry, and near 350 kHz in cryogenic temperature, confirmed by STM measurement.

The 190 nm gap, smallest sustained over millimeter-scale areas, is a large enough separation to avoid complex van der Waals interactions and roughness-induced noise, both of which become significant below 100 nm [35]. Our membranes combine high tensile stress, a superconducting transition temperature ($T_C \approx 14.2\ \text{K}$), and atomically smooth surfaces ($\approx 1\ \text{nm}$ rms roughness), all cru-

cial for precise Casimir measurements. Achieving both high T_C and high tensile stress is nontrivial, as stress typically suppresses superconductivity. Through material optimization, we preserve mechanical performance while ensuring a T_C close to bulk NbTiN. This is relevant for superconducting Casimir theories, where higher T_C improves spectral overlap between the superconducting gap and Casimir-relevant modes, enhancing the chance of measurable effects.

This fixed-gap design eliminates the need for active alignment, maintaining near-constant separation during temperature sweeps. The main deviation arises from a ~ 142 picometer sag over a 709 micron span — caused primarily by Casimir attraction — yielding an angular misalignment of just $\sim 2 \times 10^{-5}$ degrees. While active alignment of two surfaces via precision stages offers tunability, our chip-based platform achieves far superior parallelism and passive stability; ideal for temperature-based relative measurements. As a control, we fabricate an identical device with a $1.25\ \mu\text{m}$ gap, where Casimir forces are negligible (see Supplementary Information H). This allows us to disentangle Casimir-induced shifts from those caused by thermal expansion, material changes across T_C , or changes in STM readout.

Fig. 2 illustrates the extreme aspect-ratio parallelism achieved on-chip. A colorized SEM image (Fig. 2a) shows suspended NbTiN membranes with micron-scale release holes. The inset shows a side-view schematic of the Casimir cavity on a silicon substrate. A central hole (Fig. 2b) offers visual confirmation of suspension, though it is omitted in actual experiments where

vibrational modes are confirmed via laser Doppler vibrometry. Close-ups (Fig. 2c) reveal 190 nm gaps maintained over millimeter-scale areas. Fig. 2d highlights our platform’s ability to achieve extreme parallelism, defined by an unprecedented area-to-separation ratio compared to previous published Casimir experiments, using the ideal Casimir force as a metric of effective parallelism. Our system’s parallelism surpasses all previous published Casimir experiments (room-temperature and cryogenic) by orders of magnitude. Beyond small separations, our high-stress NbTiN membranes form high-Q mechanical resonators, enabling sensitive detection of Casimir shifts.

Materials engineering is central to this work. High tensile stress in NbTiN membranes prevents collapse while enabling high-Q mechanical modes for precision force sensing via dissipation dilution [36]. Years of optimization allowed us to achieve both high T_C and resilience to fabrication chemicals (see Supplementary Information B). The NbTiN stress also enhances membrane vibrational stability, making it possible to interaction with atomic-scale probes like STM. Crucially, NbTiN’s minimal oxidation allows effective in-situ annealing (to allow STM tunneling), unlike aluminum, which forms thick (~ 2 -5 nm) oxides that are difficult to remove. These properties make our platform not only well-suited for generating strong Casimir forces but also for high-precision STM interrogation, as detailed in the next section.

IV. EXPERIMENTAL SETUP AND MEASUREMENT PROTOCOL

We use a scanning tunneling microscope (STM) to measure the mechanical resonance of suspended NbTiN membranes across the superconducting transition temperature. The STM tip is positioned with sub-nanometer precision, enabling precision detection of membrane motion. By approaching within 0.3–1.0 nm of the surface, the tip tracks membrane oscillations of 30–100 pm. The tunneling current drops by a factor of 10 for every 0.1 nm increase in separation — changing by $1000\times$ over a 0.3 nm atomic diameter — making STM exquisitely sensitive to atomic-scale motion. During measurements, the tip remains confined within a ~ 10 pm lateral region — $30\times$ smaller than a Nb atom — on a $709 \times 709 \mu\text{m}^2$ membrane, spanning 12 orders of magnitude in scale. This localization enables precise cancellations of the tip’s influence on the membrane via van der Waal and electrostatic forces. Its minimal interaction area reduces disruption to the membrane’s superconductivity and enables direct measurement of the superconducting gap.

Fig. 3a shows the experimental setup. Measurements are conducted in ultra-high vacuum ($\sim 10^{-10}$ mbar) and cryogenic temperatures (4.45–14.45 K). A suspended NbTiN membrane vibrates above a fixed NbTiN backgate, driven by an AC+DC voltage (AC for actuation, DC to cancel electrostatics). Scanning tunneling mi-

croscopy (STM) detects resonance by measuring vibrational amplitude during a frequency sweep. The STM tip, mounted on a piezotube, maintains constant tunneling current and gap via feedback. At resonance, increased membrane motion reduces tip-sample distance, raises current, and triggers retraction of the tip; the resulting piezotube displacement gives the amplitude. Only the vibrational amplitude, as inferred from the average tunneling current, is recorded, since the STM’s low-noise amplifier has a cutoff frequency (~ 1 kHz) well below the membrane’s resonance frequency. The tip is optically aligned with the membrane and gradually brought into tunneling (Fig. 3b). To minimize perturbation while maintaining displacement sensitivity, it is parked 50 μm from the clamped edge, where the membrane is stiffer than at the center.

To isolate superconductivity-induced Casimir shifts from material effects and thermal expansion, we use two chips with distinct gaps: a small-gap cavity (190 nm) where Casimir forces are strong, and a large-gap cavity (1213 nm) where they are negligible. Mounting both on the same holder (Fig. 3c) ensures identical environmental conditions, enabling subtraction of material-dependent effects. Although the NbTiN films are co-deposited, we verify that both chips exhibit matched mechanical frequencies and T_C (see Supplementary Information A). This differential approach allows us to subtract shared material responses across T_C and isolate Casimir forces.

Beyond intrinsic material changes, all other extraneous forces must be minimized or eliminated, as detailed in the Methods section. Electrostatic interactions between plates are canceled via DC backgate biasing, while tip-induced forces are compensated through STM feedback. Van der Waals contributions are suppressed by tuning the tunneling current to stay in a regime where such effects are negligible. Once these known extraneous forces are removed, temperature sweeps around T_C isolate the remaining Casimir signal.

SHORT-RANGE MEASUREMENTS AROUND T_C

To probe superconductivity-induced variations in the Casimir force, we performed high-precision frequency measurements across $T_C \sim 14.2$ K. Each run began at 4.45 K, with controlled heating and stabilization at each step to minimize drift and maintain STM tip stability.

Each sweep across T_C lasted up to 16 hours with continuous stabilization and data acquisition. While open-flow helium cooling is resource-intensive (0.45 L/hour), it eliminates mechanical vibrations that would otherwise degrade STM performance and our experiments. The STM holds 9 L of liquid helium — 1.8 L for overnight tip and temperature stabilization, and 7.2 L for the T_C sweep. Ultra-high vacuum ($\sim 10^{-10}$ mbar) ensures a clean surface after annealing and suppressed squeezed-film damping at nanoscopic separations.

After systematically eliminated electrostatic forces be-

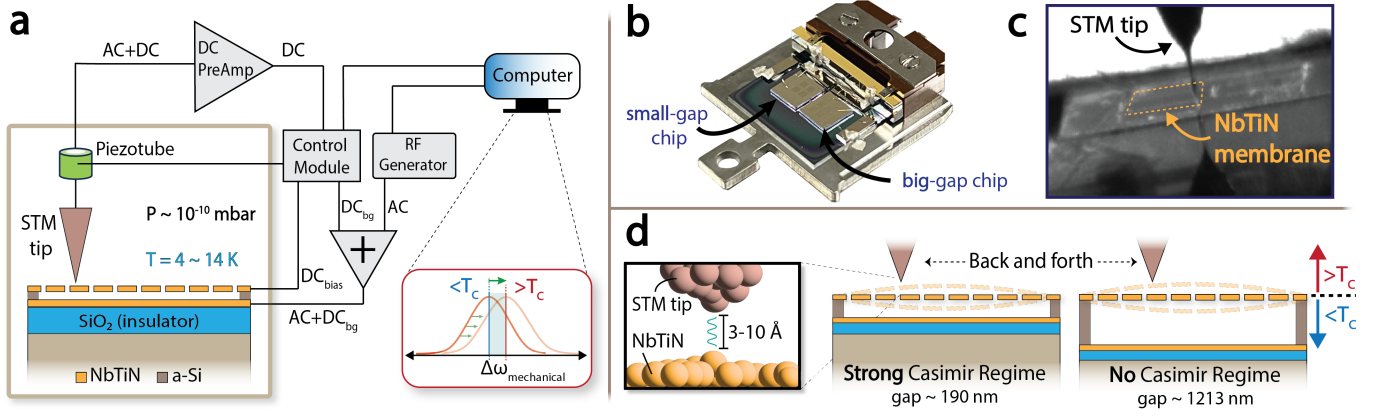


FIG. 3. STM readout of membrane motion (a) Schematic of the STM-based measurement setup, showing AC and DC signals applied to the backgate to drive the NbTiN membrane and detect resonance via tunneling with the STM tip. (b) Photo of the sample holder with wire-bonded chips featuring small (190 nm) and big (1213 nm) gaps for comparison. (c) In-situ optical image from the STM, highlighting the precise placement of the tip near the edge of the suspended membrane. (d) Protocol for detecting resonance frequency shifts induced by Casimir forces across T_C , comparing small-gap and big-gap configurations.

tween the plates and forces between the tip and membrane, we tracked membrane resonance frequency shifts, isolating Casimir contributions by comparing small-gap (190 nm) and big-gap (1213 nm) samples. Big-gap samples (with negligible Casimir force) allow us to account for any unknown changes in frequency coming from material changes at T_C , thermal expansion, or any other non-Casimir related changes. Fig. 4a shows sharper frequency shifts Δf in the small-gap cavity at $T_C \sim 14.2$ K, whereas the shifts in the big-gap cavity serve as a reference and capture shifts due to variations in mechanical properties as temperature sweeps. For consistency across runs, we define the reference value as the average frequency near 13.9 K. We use $\Delta\psi$ to denote temperature-dependent variations, and $\delta\psi$ for fixed-temperature changes in quantities ψ such as frequency or pressure. Independent resistivity measurements confirmed consistent $T_C \sim 14.2$ K across both small- and big-gap devices (Fig. 4d), using forward and backward sweeps.

Following the calibration in Supplementary Information G, we linearly fit the thermal expansion of the superconductor using data below T_C (Fig. 4a), allowing determination of the residual frequency square shift $\Delta\omega^2$ above T_C for membranes with different gaps, where $\omega = 2\pi f$ is the angular resonance frequency. Since the gap size is the only difference between membranes, we attribute the contrasting $\Delta\omega^2$ behavior to a separation-dependent force. With other distance-dependent forces minimized, we attribute the frequency shift to changes in the Casimir force. Using $\Delta\omega^2$ from the big-gap device, we estimate NbTiN's mechanical changes and compute the Casimir-induced ω^2 shift in the small-gap membrane. The relation $\Delta\omega^2 = -\Delta P'(d)/\rho t$ links frequency shift to the pressure gradient, where d is the separation, ρ the density, and t the thickness (Supplementary Information F). We extract a Casimir pressure gradient variation

of 12.10 ± 1.38 kPa/m for a 0.20 ± 0.02 K temperature change (Fig. 4c).

In our on-chip parallel-plate setup, the combination of large area and small gap d yields a strong Casimir force, enabling high sensitivity to small variations [37]. This amplifies superconductivity-induced changes, resulting in a pronounced fractional frequency shift that scales with the pressure and force gradients: $\Delta f/f \approx -\Delta P'_{\text{Cas}} L^2 / (4\pi^2 \sigma t) = -\Delta F'_{\text{Cas}} / (4\pi^2 \sigma t)$ (Supplementary Information F).

Based on Lifshitz theory [14], we estimate that near T_C , the Casimir pressure on the suspended NbTiN membrane at a 190 nm separation fits as $P_{\text{Cas}}|_{d=190\text{nm}} = -1.081 \times 10^{-24} / d^{3.507}$ [Pa] ≈ -0.403 Pa (with d in meters; negative sign denotes attraction). Using this fit, a finite element simulation estimated that the measured ω^2 variation (Fig. 4b) corresponds to a Casimir force change of $\Delta F_{\text{Cas}} = -0.33 \pm 0.04$ nN, or equivalently, a pressure change of $\Delta P_{\text{Cas}} = -0.65 \pm 0.07$ mPa across the transition. The negative signs indicate that both force and pressure increase as temperature rises through T_C . Further studies across different gap sizes are needed to clarify this behavior.

The abrupt change in Casimir pressure gradient across T_C in Fig. 4c was not predicted by existing theory [14]. Since the Casimir force is the derivative of the Helmholtz free energy, $F_{\text{Cas}} = -\partial \mathcal{F} / \partial d$ [38], it is expected to remain continuous through a second-order phase transition. Furthermore, the smooth convergence of BCS and Drude permittivity models at T_C supports a continuous force (see Supplementary Information H).

A possible explanation links this behavior to the long-standing Drude-plasma model debate, which centers on the zero-frequency ($n = 0$) Matsubara term in the Lifshitz formula. The Drude model predicts a vanishing transverse electric (TE) contribution, while the plasma

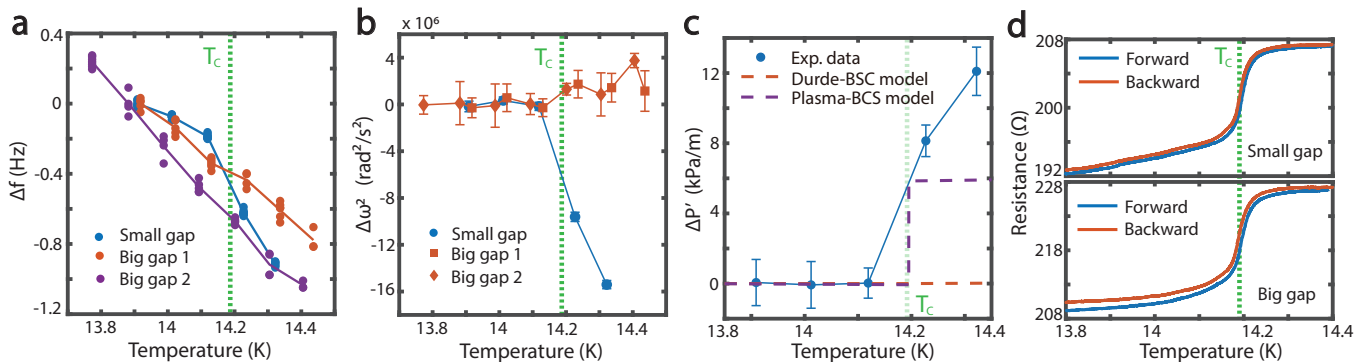


FIG. 4. (a) Membrane frequency vs. temperature near $T_C \approx 14.2$ K for one small-gap sweep and two big-gap sweeps. (b) Frequency square shift $\Delta\omega^2$ after calibrating out the temperature dependence of the elastic force (see Supplementary Information G), showing contrasting behavior between small- and big-gap membranes. (c) Pressure gradient variation for the 190 nm-gap membrane. Data (blue dots) are compared with Casimir pressure predictions using the BCS model for ($T < T_C$) and either Drude (red) or plasma (purple) models for ($T > T_C$) (Supplementary Information H). (d) Forward and backward resistivity sweeps confirm ($T_C \sim 14.2$ K) for both membranes.

model allows a finite one that significantly affects the force. While room-temperature experiments favor the plasma model, confirmation in cryogenic regimes — especially for superconductors — remains lacking. To reconcile our observation, we propose a hybrid model using the plasma prescription for $T > T_C$ and the BCS permittivity for $T < T_C$, resulting in a changing zero-frequency term and a discontinuous pressure gradient (the “Plasma-BCS” model). For comparison, we also consider a Drude-BCS model, which yields a continuous gradient. Both predictions appear in Fig. 4c. Notably, only the Plasma-BCS model reproduces the magnitude of our experimental signal, suggesting it may capture the essential physics.

In Fig. 4c we use $\Omega = 5.33$ eV/ \hbar , consistent with NbTiN estimates [14], but reproducing the full jump requires $\Omega = 12.7$ eV/ \hbar . Because the zero-frequency contribution is poorly understood, Ω need not match the infrared-derived plasma frequency. A full discussion is provided in Supplementary Information H. If confirmed, this jump would mark a major advance — representing the first measurement sensitive to a transition in the zero-frequency permittivity term across a phase transition, and deepening our understanding of dissipation and quantum fluctuations.

Our results highlight the importance of extreme parallelism, compliant mechanics, advanced material engineering, and high-precision readout in isolating subtle Casimir force variations. While initial findings are promising, further studies are needed with finer temperature sweeps, varying gap sizes, thicknesses, and superconducting materials to better constrain theory. Future work will focus on reproducibility and model refinement, leveraging our platform’s unique sensitivity to probe Casimir-superconductivity interactions.

V. CONCLUSION AND OUTLOOK

The interplay between Casimir forces and superconductivity remains an open frontier in quantum physics, with implications for longstanding debates on electron physics, high- T_C superconductivity, and perhaps quantum gravity. We introduced a microchip-based platform that achieves extreme parallelism and mechanical stability, enabling high-precision Casimir force measurements across T_C . Compared to previous superconducting Casimir experiments across T_C [16, 17], our system increases the interacting surface area by over three orders of magnitude and achieves pressure resolutions 100 times greater. The generated Casimir forces exceed the average of all previously published Casimir measurements by more than two orders of magnitude (Supplementary Information J).

Our approach eliminates thermal, electrostatic, and van der Waals contributions while operating at cryogenic temperatures. We introduce a novel STM readout that directly detects membrane resonance, extending STM’s role from atomic imaging to mesoscopic force sensing. Its highly localized interaction area minimizes disruption to superconductivity and allows precise cancellation of tip-induced forces.

Initial measurements reveal frequency shifts in small-gap membranes near T_C , consistent with superconductivity-modulated Casimir interactions. If due to Casimir effects, this would be the first evidence that superconductivity alters vacuum fluctuations. The sign of the shift suggests a *decrease* in Casimir pressure across T_C , contrary to expectations, and the abruptness appears inconsistent with a second-order phase transition. Existing theory [14] predicts a smooth change, while a model using the plasma prescription for the $n = 0$ Matsubara term in the normal state [39–43] reproduces our result to similar order of magnitude. As this prescription aligns with room-temperature Casimir

data, its extension to the superconducting regime is a plausible hypothesis. Nonetheless, broader sweeps and gap variation are needed to verify the trend and rule out alternative causes.

Though our approach sets a new benchmark, further gains in parallelism are limited by stiction from residual charge, motivating collapse recovery methods [44] and the exploration of higher- T_C superconductors. Beyond Casimir physics, our platform offers broad utility for sensing, table-top quantum gravity [45], and condensed matter experiments [46]. Its extreme parallelism enhances responsivity via Casimir forces [37], enabling applications in accelerometry [47], optomechanics [48], and other force-sensitive systems.

These results highlight the potential of combining on-chip nanomechanics and STM to probe fundamental quantum effects — opening a new experimental regime where superconductivity and vacuum fluctuations begin to interact.

VI. METHODS

A. STM measurement protocol

After fabricating the solid-state parallel-plate cavities, we use a scanning tunneling microscope (STM) to measure membrane dynamics with atomic-scale precision. While STM is typically used for atomic imaging and transport studies on ultra-flat surfaces, its extreme sensitivity to tip-sample distance makes it ideal for detecting nanomechanical motion. The tunneling current depends exponentially on separation, with 0.1 nm changes producing an order-of-magnitude variation. Here, we repurpose STM to track the mechanical resonance of suspended superconducting NbTiN membranes, extending its use from atomic-scale measurements to mesoscopic devices.

Two aspects of the STM’s atomic-scale precision are critical for our measurements. First, its high vertical (z) resolution enables detection of membrane resonance by tracking oscillation-induced changes in tunneling current as the membrane resonantly vibrates within tunneling distance. Second, its lateral (x/y) precision — maintained by dual feedback loops — keeps the tip fixed at the same membrane location throughout, ensuring reproducibility by avoiding spatial variation in local forces.

The STM’s signal control is handled by a Nanonis™ system, which applies both a bias voltage (V_{bias}) and a backgate voltage (V_{bg}), while positioning the tip based on the measured tunneling current. The backgate voltage is combined with an oscillating voltage V_{AC} from an RF generator (Rohde & Schwarz SMB100A) via a bias tee (Mini-Circuits ZFBT-4R2GW+) and applied to the bottom NbTiN film. The bias voltage is applied to the suspended NbTiN membrane, producing a tunneling current when the STM tip is nearby. Because the tip-membrane conductance depends exponentially on their separation, membrane oscillations modulate the tunneling current.

This oscillating current is then amplified by a low-noise current amplifier (NF Corp. SA-607F2). Because the amplifier’s cutoff frequency is well below the membrane’s resonance frequency, the amplifier effectively converts the oscillating tunneling current into an averaged DC current output that is recorded by the control system.

By setting fixed values for the tunneling current and bias voltage, the system controls the distance between the tip apex and the membrane. When V_{AC} is applied to the backgate, the membrane is driven, and its vibrational amplitude increases the most as the AC signal approaches the membrane’s mechanical resonance frequency. To maintain a constant averaged tunneling current, the STM tip retracts, adjusting its z -position via the piezoceramic tube. This z -position is then recorded by the control system, providing a direct measure of the membrane’s vibrational amplitude. When the AC signal frequency nears the resonant frequency of the nanomembrane, the increased vibrational amplitude is clearly resolved in the tip’s z -position, thereby indicating both the resonance position and the mode amplitude as seen in Fig. 5c.

The STM offers several key advantages for this unconventional application. Unlike optical or capacitive readouts, which can perturb the membrane over large areas and billions of atoms, STM tunneling is extremely localized and equally effective above and below T_C , making it ideal for studying the superconducting transition. Furthermore, the ultra-high vacuum (UHV) environment required for cryogenic STM operation provides exceptional control over surface conditions. Our STM has annealing capabilities that reduce surface oxidation — an often-overlooked factor in cryogenic nanomechanical setups. NbTiN resists oxidation far better than aluminum [16, 29, 33] due to its stable nitride structure, which limits oxygen diffusion. Unlike aluminum oxides, which are chemically stable and difficult to remove, NbTiN oxidation remains minimal and can be effectively annealed in ultra-high vacuum at 200°C, ensuring a cleaner superconducting surface for STM measurements and removing a source of electrostatic patch potentials [12, 13]. The STM tip can directly probe superconducting properties by identifying the superconducting gap and T_C , offering a complementary diagnostic tool alongside mechanical measurements. In addition to its high T_C , these characteristics highlight NbTiN’s suitability as a membrane material — its surface compatibility with STM enables robust coupling between the mechanical structure and the tunneling readout. Casimir forces are inherently surface-dominated, as are many noise sources, making STM an ideal probe; here, we demonstrate its dual role in both mechanical detection and direct surface characterization, offering insights inaccessible to conventional methods.

Our measurement protocol is designed to detect changes in the Casimir force across the superconducting transition by tracking shifts in the mechanical resonance frequency of suspended membranes. Rather than

measuring absolute Casimir forces — which are subject to large theoretical uncertainties due to unknown superconducting corrections and thermal contributions — we focus on relative changes across T_C . This differential approach enhances sensitivity to superconductivity-induced modifications of the Casimir interaction. Small-gap (190 nm) and big-gap (1213 nm) configurations are compared to isolate Casimir-specific effects, with the big-gap device serving as a control to subtract out non-Casimir contributions such as thermal expansion, changes in the material, and changes in the tunneling across T_C . STM's high spatial precision enables stable, reproducible readout on both devices, providing high-confidence removal of non-Casimir effects.

The experimental setup consists of a loadlock, a preparation chamber, and a measurement chamber. Samples are first loaded into the loadlock and annealed at 200°C under a pressure of 1.7×10^{-8} mbar for two days to remove contaminants. They are then transferred to the preparation and measurement chambers, where experiments are performed at 4.45 K and 1.5×10^{-9} mbar. As shown in Fig. 3b, the sample holder accommodates chips with both small- and big-gap cavities, allowing side-by-side comparison. AC and DC signals are applied to the backgate beneath the membranes to drive mechanical oscillations and cancel electrostatic forces. A bias voltage on the suspended membrane enables tunneling current detection by the STM tip. Tip placement is guided by an in-situ optical camera (Fig. 3b), enabling coarse positioning near the membrane edge (60 microns away) where vibrational amplitude is minimized. Resonance frequency measurements are then performed at different temperatures across T_C .

By combining our novel STM readout with microchip-based Casimir cavities, we establish a powerful platform for minimally invasive, high-sensitivity measurements across the superconducting transition. Achieving meaningful results, however, requires careful isolation of all extraneous forces that could obscure the Casimir effect—including those introduced by the STM, electrostatic interactions between the plates, and thermal expansion or unknown material changes at T_C during temperature sweeps. In the following section, we outline the methods used to systematically eliminate these contributions, allowing us to isolate signals attributable to the Casimir force.

B. Experimentally Isolating Casimir Forces

To isolate the Casimir force in our solid-state parallel-plate cavities, we systematically eliminate other forces acting on the superconducting membrane, including electrostatic attractions, van der Waals (VdW) interactions, and thermal-elastic effects from temperature sweeps across T_C . Our protocol begins by canceling electrostatic forces between the membrane and backgate, followed by tip-membrane electrostatics, and finally minimizing

VdW interactions. Combined with precise STM positioning and detailed temperature control, this sequence enables reproducible, high-sensitivity measurements of Casimir forces across the superconducting transition.

C. Positioning and Minimizing Tip-Membrane Forces

As shown in Fig. 5a, the STM's enables to scan the surface of the membrane within a $3 \times 3 \text{ nm}^2$ area, effectively imaging the mechanical resonator at the scale of individual atoms. The surface lacks crystalline smoothness due to sputtering growth. The resulting roughness of 1-2 nm results in high and low points in the scan window. By combining the STM's current-to-tip height feedback system with a local gradient search algorithm, the STM autonomously locks onto the locally highest point with 10 pm precision — nearly 30 times smaller than the 300 pm radius of a niobium atom on the NbTiN membrane (see inset Fig. 5a). This remarkable sub-atomic spatial resolution ensures the tip remains fixed at the same membrane location throughout measurements, minimizing positional drift and enhancing reproducibility. This level of precision ensures that the local force environment remains stable and consistent throughout measurements. While tunneling current depends exponentially on tip-sample separation, simply maintaining a constant current at a different location would not guarantee identical forces. By fixing the tip at the same membrane position with sub-atomic precision, we minimize variations in local interactions, ensuring reproducible force measurements. With this sub-atomic localization, the STM provides extreme control over how our measurements interact with the experimental system. This control is essential for precisely canceling out any perturbative effects introduced by the measurement process.

D. Mitigating Electrostatic Forces

Electrostatic interactions—arising from residual surface charges and contact potential differences—pose a significant challenge in Casimir experiments. Because electrostatic forces scale as $F_{\text{ES}} \propto A/d^2$ in plate-plate geometries, they directly compete with the Casimir force and must be experimentally eliminated. These forces stem from sources such as surface contamination, grain boundaries, or static charges from fabrication or air exposure, making them difficult to predict or model [11–13]. Therefore, in Casimir experiments they must be removed experimentally, as they contribute in unknown ways at small separations.

To cancel electrostatic forces between the membrane and the backgate, we measure the membrane's resonance frequency as a function of backgate voltage for both small- and big-gap cavities (Fig. 5c). The apex of the

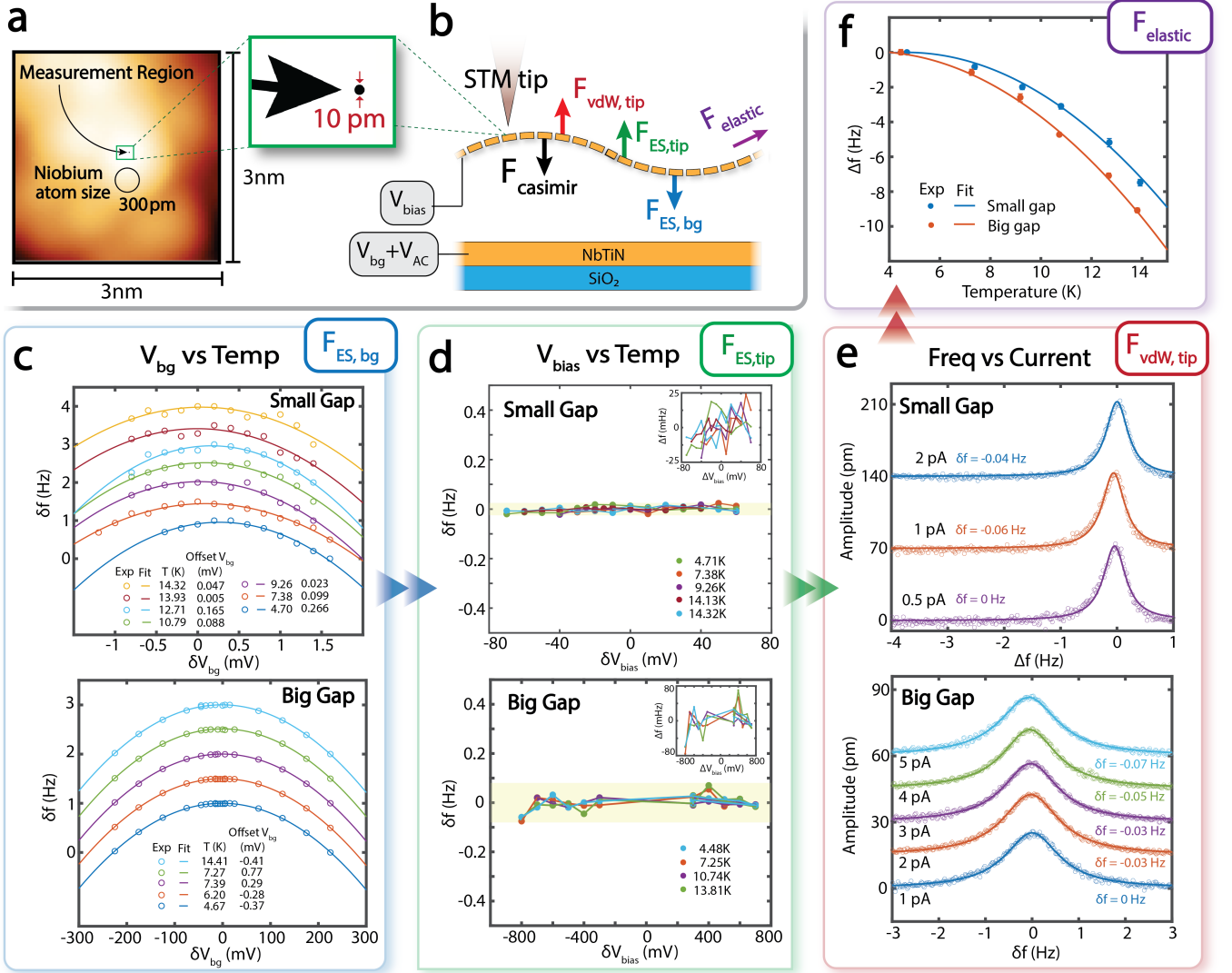


FIG. 5. Eliminating non-Casimir Effects with STM-Microchip Approach (a) Atomic-scale scan (3 × 3 nm²) showing the surface topology of the NbTiN membranes, demonstrating the STM's ability to achieve sub-atomic spatial resolution (down to 10 pm, smaller than the diameter of an atom) during measurements. (b) STM positioned above the Casimir cavity membrane, requiring the elimination of forces associated with the tip-sample interaction (red, green), electrostatics between the plates (blue), and thermal-elastic effects from temperature sweeps (purple). All forces are canceled in small- and big-gaps device as plotted in the following: (c) Frequency response as a function of backgate voltage to compensate for electrostatic forces between the plates by finding the apex of the parabola. Subplots in the panel were manually spaced for clarity. (d) Frequency response as a function of tip-membrane bias voltage, used to eliminate residual electrostatic forces between the tip and membrane. The shaded areas (yellow) show the range of the frequency shift, which are presented in the insets. (e) Frequency response of membranes over small (top) and big (bottom) gaps as a function of current, used to minimize van der Waals forces between the tip and the membrane. Subplots in the panel were manually spaced for clarity. (f) Final stage: performing large span temperature sweeps to attain elastic contributions from thermal expansion coefficients.

resulting parabola identifies the voltage that minimizes the electrostatic interaction. This compensation voltage is used throughout temperature sweeps to keep the membrane-backgate force balanced.

Temperature sweeps and corresponding measurements on both small- and big-gap membranes show that the apex voltage shifts by less than 0.2 mV (small-gap) and 1.1 mV (big-gap). Finite element simulations trans-

late these into pressure differences of 4.9×10^{-6} Pa and 3.6×10^{-6} Pa, and frequency shifts of 2.6×10^{-3} Hz and 2.6×10^{-4} Hz, respectively—close to the sensitivity limit of our experiment. These small shifts indicate that the electrostatic potential remains stable during temperature sweeps. For subsequent measurements, we fixed the backgate voltage at 257.2 mV (small-gap) and 223.6 mV (big-gap), ensuring electrostatic cancellation without compro-

missing sensitivity.

To minimize electrostatic forces between the STM tip and the membrane, the tip-membrane bias voltage is swept while maintaining constant tip-sample separation. The resonance frequency response is monitored to identify the compensation voltage where residual interactions vanish (Fig. 5d). This procedure ensures that tip-induced electrostatic forces remain negligible throughout measurements.

E. Tip-membrane van der Waals forces

As the STM tip approaches the membrane, VdW forces between the tip and membrane can become significant. To mitigate this, the STM tip is sharpened and cleaned by dipping it into a copper sample and applying voltage pulses. Atomic steps on the copper surface are imaged to verify sharpness, ensuring the tip's outermost atoms are well-defined. While this method confirms the presence of a clean, localized apex, it does not fully characterize the sharpness beyond this range, as additional atomic-scale features — such as dangling atoms — may still be present. The optimal landing spot on the membrane is then identified as the highest, most stable location to minimize position-dependent van der Waals interactions during temperature sweeps. The membrane's resonance frequency response is validated at different tip-membrane currents (i.e. different tip-membrane distances) to ensure Lorentzian mechanical peaks, confirming that van der Waals forces are minimized (Fig. 5e); the lack of frequency shift across these distances indicates that distance-dependent VdW contributions are negligible within our measurement uncertainty.

F. Managing Thermal Drift and Elastic Forces

Temperature sweeps introduce thermal drift and elastic effects that can distort measurements if not properly managed. To address this, we begin at the base temperature (4.45 K) with a precise $3 \times 3 \text{ nm}^2$ scan of the membrane. Drift is actively corrected using the STM's scanning capabilities at atomic scales and feedback system operating at frequencies up to 50 Hz, maintaining a lateral tip position to within a 10 pm region during resonance sweeps.

As the temperature increases, thermal expansion induces additional drift, which is mitigated by incremental heating and stabilization protocols. For temperature spans of 0.1 K, 1 K, and 5 K, stabilization times of 1 hour, 2.5 hours, and 3 hours, respectively, are employed to maintain precise alignment. These steps ensure that thermal-elastic effects are systematically accounted for during temperature-dependent measurements.

Following the compensation of electrostatic forces and van der Waals and forces, the system is prepared for long-range temperature sweeps to study Casimir force varia-

tions from a base temperature of 4.45 K to the superconducting transition temperature, $T_C \sim 14.2 \text{ K}$. These large sweeps provide an overall understanding of how the forces between the plates evolve over a broad temperature range, albeit with reduced stability compared to small-range sweeps near T_C . The minimized residual interactions, combined with the STM's high sensitivity, establish a robust platform for detecting subtle changes in the Casimir force.

However, measuring Casimir force differences over large temperature spans introduces additional challenges. These include variability in the mechanical properties of the NbTiN membranes, shifts in the tip landing position, and increased thermalization time requirements, all of which can influence interaction consistency. For this reason, the most critical measurements are conducted over small temperature ranges near the superconducting transition, where the interplay between superconductivity and the Casimir force is perhaps more prominent. As illustrated in Fig. 5f, large sweeps serve as a broader diagnostic tool, while precision measurements across T_C provide the most meaningful insights into the behavior of the Casimir force in superconducting systems.

For comparison, Supplementary Information C includes cases where the tip-membrane interaction is moderately larger or significantly stronger. These examples highlight the critical importance of minimizing VdW and electrostatic forces to ensure reliable Casimir force measurements. All of these procedures are performed for every experimental run across T_C . By achieving these conditions, our experimental setup is optimized for detecting subtle variations in the Casimir force.

ACKNOWLEDGMENTS

We thank Peter Steeneken, Shahrukh Ashruf, and Noud Derks for help with analysis; Martin Lee for early cleanroom support, along with Charles de Boer, Marinus Fischer, Bas van Asten, Pauline Stevic, and Roald van der Kolk. We are grateful to Allard Katan, Alexandre Artaud, Evert Stolte, Ronald Bode, and Tino Kool for measurement support. We also thank Yufan Li, Zichao Li, Hanqing Liu, Ruben Guis, Martijn Veen, Andrea Cupertino, Vidharshana Sivakumar, and Junho Suh for their contributions, and Martin Tajmar, James Quach, Nathan Inan, Farbod Alijani, Achim Kempf, Gerard Verbiest, and Peter Steeneken for valuable feedback on the manuscript. This publication is part of the project, Probing the physics of exotic superconductors with microchip Casimir experiments (740.018.020) of the research programme NWO Start-up which is partly financed by the Dutch Research Council (NWO). Funded/Co-funded by the European Union (ERC, EARS, 101042855). Views and opinions expressed are however those of the author(s) only and do not necessarily reflect those of the European Union or the European Research Council.

-
- [1] H. B. Casimir, In *Proc. Kon. Ned. Akad. Wet.*, volume 51. **1948** 793.
- [2] S. K. Lamoreaux, *Physical Review Letters* **1997**, *78*, 1 5.
- [3] J. Bardeen, L. N. Cooper, J. R. Schrieffer, *Physical review* **1957**, *108*, 5 1175.
- [4] T. Gong, B. Spreng, M. Camacho, I. Liberal, N. Engheta, J. N. Munday, *Physical Review A* **2022**, *106*, 6 062824.
- [5] G. Torricelli, P. Van Zwol, O. Shpak, C. Binns, G. Palasantzas, B. Kooi, V. Svetovoy, M. Wuttig, *Physical Review A—Atomic, Molecular, and Optical Physics* **2010**, *82*, 1 010101.
- [6] G. Bressi, G. Carugno, R. Onofrio, G. Ruoso, *Physical review letters* **2002**, *88*, 4 041804.
- [7] K. Y. Fong, H.-K. Li, R. Zhao, S. Yang, Y. Wang, X. Zhang, *Nature* **2019**, *576*, 7786 243.
- [8] M. Šiškins, M. Lee, S. Mañas-Valero, E. Coronado, Y. M. Blanter, H. S. van der Zant, P. G. Steeneken, *Nature communications* **2020**, *11*, 1 2698.
- [9] O. Suchoi, E. Buks, *Europhysics Letters* **2017**, *117*, 5 57008.
- [10] C. Binek, *Scientific Reports* **2017**, *7*, 1 1.
- [11] D. Garcia-Sanchez, K. Y. Fong, H. Bhaskaran, S. Lamoreaux, H. X. Tang, *Physical Review Letters* **2012**, *109*, 2 027202.
- [12] M. Liu, R. Schafer, J. Xu, U. Mohideen, *Modern Physics Letters A* **2020**, *35*, 03 2040001.
- [13] J. L. Garrett, J. Kim, J. N. Munday, *Physical Review Research* **2020**, *2*, 2 023355.
- [14] G. Bimonte, *Physical Review A* **2019**, *99*, 5 052507.
- [15] G. Klimchitskaya, V. Mostepanenko, *Modern Physics Letters A* **2020**, *35*, 03 2040007.
- [16] R. A. Norte, M. Forsch, A. Wallucks, I. Marinković, S. Gröblacher, *Physical review letters* **2018**, *121*, 3 030405.
- [17] H. Eerkens, Ph.D. thesis, Ph. D. thesis, Leiden University, **2017**.
- [18] S. Avino, A. Basti, E. Calloni, S. Caprara, M. de Laurentis, R. de Rosa, L. Errico, G. Esposito, F. Frasconi, G. Gagliardi, et al., In *Gravitational-waves Science&Technology Symposium*. **2018** 020.
- [19] E. Calloni, L. Di Fiore, G. Esposito, L. Milano, L. Rosa, *Physics Letters A* **2002**, *297*, 5-6 328.
- [20] S. A. Fulling, K. A. Milton, P. Parashar, A. Romeo, K. Shajesh, J. Wagner, *Physical Review D—Particles, Fields, Gravitation, and Cosmology* **2007**, *76*, 2 025004.
- [21] G. Bimonte, E. Calloni, G. Esposito, L. Rosa, *Physical Review D—Particles, Fields, Gravitation, and Cosmology* **2006**, *74*, 8 085011.
- [22] J. Q. Quach, *Physical Review Letters* **2015**, *114*, 8 081104,
Note: While the published version of this work suggested that gravitational Casimir forces could exceed electromagnetic Casimir forces, follow-up analysis and private communication with the authors indicate that key aspects of the model remain unresolved. Current estimates, based on revised assumptions about reflectivity and cutoff frequencies, suggest the effect may be several orders of magnitude smaller and perhaps immeasurable with modern experimental techniques.
- [23] D. Pérez-Morelo, A. Stange, R. W. Lally, L. K. Barrett, M. Imboden, A. Som, D. K. Campbell, V. A. Aksyuk, D. J. Bishop, *Microsystems & nanoengineering* **2020**, *6*, 1 115.
- [24] A. Kempf, *Journal of Physics A: Mathematical and Theoretical* **2008**, *41*, 16 164038.
- [25] M. Orlando, A. Rouver, J. Rocha, A. Cavichini, *Physics Letters A* **2018**, *382*, 22 1486.
- [26] M. Strongin, O. Kammerer, *Journal of Applied Physics* **1968**, *39*, 6 2509.
- [27] M. Strongin, O. Kammerer, J. Crow, R. Parks, D. Douglass Jr, M. Jensen, *Physical Review Letters* **1968**, *21*, 18 1320.
- [28] A. W. Rodriguez, P.-C. Hui, D. P. Woolf, S. G. Johnson, M. Lončar, F. Capasso, *Annalen der Physik* **2015**, *527*, 1-2 45.
- [29] R. Andrews, A. Reed, K. Cicak, J. Teufel, K. Lehnert, *Nature communications* **2015**, *6*, 1 10021.
- [30] L. Tang, M. Wang, C. Ng, M. Nikolic, C. T. Chan, A. W. Rodriguez, H. B. Chan, *Nature Photonics* **2017**, *11*, 2 97.
- [31] M. Wang, L. Tang, C. Ng, R. Messina, B. Guizal, J. Crosse, M. Antezza, C. T. Chan, H. B. Chan, *Nature communications* **2021**, *12*, 1 600.
- [32] J. M. Pate, M. Goryachev, R. Y. Chiao, J. E. Sharping, M. E. Tobar, *Nature Physics* **2020**, *16*, 11 1117.
- [33] M. H. de Jong, E. Korkmazgil, L. Banniard, M. A. Sillanpää, L. M. de Lépinay, *arXiv preprint arXiv:2501.13759* **2025**.
- [34] G. Bimonte, D. Born, E. Calloni, G. Esposito, U. Huebner, E. Il'ichev, L. Rosa, F. Tafuri, R. Vaglio, *Journal of Physics A: Mathematical and Theoretical* **2008**, *41*, 16 164023.
- [35] P. Van Zwol, G. Palasantzas, M. Van De Schootbrugge, J. T. M. De Hosson, *Applied Physics Letters* **2008**, *92*, 5.
- [36] S. Schmid, K. Jensen, K. Nielsen, A. Boisen, *Physical Review B—Condensed Matter and Materials Physics* **2011**, *84*, 16 165307.
- [37] J. Javor, Z. Yao, M. Imboden, D. K. Campbell, D. J. Bishop, *Microsystems & nanoengineering* **2021**, *7*, 1 73.
- [38] G. Bimonte, T. Emig, M. Kardar, M. Krüger, *Annual Review of Condensed Matter Physics* **2017**, *8*, 1 119.
- [39] R. Decca, D. López, E. Fischbach, G. Klimchitskaya, D. Krause, V. Mostepanenko, *The European Physical Journal C* **2007**, *51* 963.
- [40] C.-C. Chang, A. Banishev, R. Castillo-Garza, G. Klimchitskaya, V. Mostepanenko, U. Mohideen, *Physical Review B—Condensed Matter and Materials Physics* **2012**, *85*, 16 165443.
- [41] A. Banishev, G. Klimchitskaya, V. Mostepanenko, U. Mohideen, *Physical Review Letters* **2013**, *110*, 13 137401.
- [42] G. Bimonte, D. López, R. S. Decca, *Physical Review B* **2016**, *93*, 18 184434.
- [43] G. Bimonte, B. Spreng, P. A. Maia Neto, G.-L. Ingold, G. L. Klimchitskaya, V. M. Mostepanenko, R. S. Decca, *Universe* **2021**, *7*, 4 93.
- [44] E. Buks, M. L. Roukes, *Europhysics Letters* **2001**, *54*, 2 220.

- [45] M. F. Gely, G. A. Steele, *AVS Quantum Science* **2021**, 3, 3.
- [46] T. J. Maldonado, D. N. Pham, A. Amaolo, A. W. Rodriguez, H. E. Türeci, *Physical Review B* **2024**, 110, 1 014508.
- [47] M. Yuan, V. Singh, Y. M. Blanter, G. A. Steele, *Nature communications* **2015**, 6, 1 8491.
- [48] A. Youssefi, M. Chegnizadeh, M. Scigliuzzo, T. J. Kippenberg, *arXiv preprint* **2025**, *arXiv:2501.03211*.
- [49] T. Kimoto, J. A. Cooper, *Fundamentals of Silicon Carbide Technology: Growth, Characterization, Devices and Applications*, Wiley-IEEE Press, **2014**.
- [50] U. Leonhardt, *Philosophical Transactions of the Royal Society A* **2020**, 378, 2177 20190229.
- [51] C. Villarreal, S. F. Caballero-Benitez, *Physical Review A* **2019**, 100, 4 042504.
- [52] S. K. Sahu, J. Vaidya, F. Schmidt, D. Jangade, A. Thamizhavel, G. Steele, M. M. Deshmukh, V. Singh, *2D Materials* **2019**, 6, 2 025027.
- [53] G. Bimonte, E. Calloni, G. Esposito, L. Rosa, *Nuclear physics B* **2005**, 726, 3 441.
- [54] D. K. Campbell, I. Bouche, A. Som, D. J. Bishop, *arXiv preprint arXiv:2412.10179* **2024**.
- [55] A. Allocca, G. Bimonte, D. Born, E. Calloni, G. Esposito, U. Huebner, E. Il'ichev, L. Rosa, F. Tafuri, *Journal of superconductivity and novel magnetism* **2012**, 25 2557.
- [56] J. Clarke, F. K. Wilhelm, *Nature* **2008**, 453, 7198 1031.
- [57] H.-W. Lee, K.-C. Kim, J. Lee, *IEEE transactions on magnetics* **2006**, 42, 7 1917.
- [58] A. B. Abrahamsen, N. Mijatovic, E. Seiler, T. Zirngibl, C. Træholt, P. B. Nørgård, N. F. Pedersen, N. H. Andersen, J. Østergaard, *Superconductor Science and Technology* **2010**, 23, 3 034019.
- [59] T. Padmanabhan, *International Journal of Modern Physics D* **2006**, 15, 12 2029.
- [60] L. Rosa, S. Avino, E. Calloni, S. Caprara, M. De Laurentis, R. De Rosa, G. Esposito, M. Grilli, E. Majorana, G. Pepe, et al., *The European Physical Journal Plus* **2017**, 132 1.
- [61] G. Binnig, H. Rohrer, C. Gerber, E. Weibel, *Applied Physics Letters* **1982**, 40, 2 178.
- [62] P. Van Zwol, G. Palasantzas, J. T. M. De Hosson, *Physical Review B—Condensed Matter and Materials Physics* **2008**, 77, 7 075412.
- [63] S. S. Verbridge, J. M. Parpia, R. B. Reichenbach, L. M. Bellan, H. G. Craighead, *Journal of Applied Physics* **2006**, 99, 12.
- [64] A. W. Rodriguez, F. Capasso, S. G. Johnson, *Nature photonics* **2011**, 5, 4 211.
- [65] A. Youssefi, S. Kono, A. Bancora, M. Chegnizadeh, J. Pan, T. Vovk, T. J. Kippenberg, *Nature* **2022**, 612, 7941 666.
- [66] A. Youssefi, S. Kono, M. Chegnizadeh, T. J. Kippenberg, *Nature Physics* **2023**, 19, 11 1697.
- [67] M. Chegnizadeh, M. Scigliuzzo, A. Youssefi, S. Kono, E. Guzovskii, T. J. Kippenberg, *Science* **2024**, 386, 6728 1383.
- [68] U. Mohideen, A. Roy, *Physical Review Letters* **1998**, 81, 21 4549.
- [69] H. B. Chan, V. A. Aksyuk, R. N. Kleiman, D. J. Bishop, F. Capasso, *Science* **2001**, 291, 5510 1941.
- [70] R. Decca, D. López, E. Fischbach, D. Krause, *Physical review letters* **2003**, 91, 5 050402.
- [71] R. Decca, D. López, E. Fischbach, G. Klimchitskaya, D. Krause, V. Mostepanenko, *Physical Review D—Particles, Fields, Gravitation, and Cosmology* **2007**, 75, 7 077101.
- [72] J. Munday, F. Capasso, V. A. Parsegian, S. M. Bezrukov, *Physical Review A—Atomic, Molecular, and Optical Physics* **2008**, 78, 3 032109.
- [73] G. Jourdan, A. Lambrecht, F. Comin, J. Chevrier, *Europhysics Letters* **2009**, 85, 3 31001.
- [74] S. De Man, K. Heeck, R. Wijngaarden, D. Iannuzzi, *Physical review letters* **2009**, 103, 4 040402.
- [75] M. Masuda, M. Sasaki, *Physical review letters* **2009**, 102, 17 171101.
- [76] J. N. Munday, F. Capasso, V. A. Parsegian, *Nature* **2009**, 457, 7226 170.
- [77] G. Torricelli, I. Pirozhenko, S. Thornton, A. Lambrecht, C. Binns, *Europhysics Letters* **2011**, 93, 5 51001.
- [78] A. Sushkov, W. Kim, D. Dalvit, S. Lamoreaux, *Nature Physics* **2011**, 7, 3 230.
- [79] A. Banishev, G. Klimchitskaya, V. Mostepanenko, U. Mohideen, *Physical Review Letters* **2013**, 110, 13 137401.
- [80] D. Ether, L. Pires, S. Umrath, D. Martinez, Y. Ayala, B. Pontes, G. d. S. Araújo, S. Frases, G.-L. Ingold, F. Rosa, et al., *Europhysics Letters* **2015**, 112, 4 44001.
- [81] G. Bimonte, D. López, R. S. Decca, *Physical Review B* **2016**, 93, 18 184434.
- [82] J. L. Garrett, D. A. Somers, J. N. Munday, *Physical review letters* **2018**, 120, 4 040401.
- [83] J. Xu, G. Klimchitskaya, V. Mostepanenko, U. Mohideen, *Physical Review A* **2018**, 97, 3 032501.
- [84] M. Liu, J. Xu, G. Klimchitskaya, V. Mostepanenko, U. Mohideen, *Physical Review B* **2019**, 100, 8 081406.
- [85] A. Stange, M. Imboden, J. Javor, L. K. Barrett, D. J. Bishop, *Microsystems & nanoengineering* **2019**, 5, 1 14.
- [86] M. Liu, J. Xu, G. Klimchitskaya, V. Mostepanenko, U. Mohideen, *Physical Review A* **2019**, 100, 5 052511.
- [87] M. Liu, Y. Zhang, G. Klimchitskaya, V. Mostepanenko, U. Mohideen, *Physical Review Letters* **2021**, 126, 20 206802.
- [88] L. B. Pires, D. S. Ether, B. Spreng, G. R. d. S. Araújo, R. S. Decca, R. Dutra, M. Borges, F. S. Rosa, G.-L. Ingold, M. J. Moura, et al., *Physical Review Research* **2021**, 3, 3 033037.
- [89] M. Liu, Y. Zhang, G. Klimchitskaya, V. Mostepanenko, U. Mohideen, *Physical Review B* **2021**, 104, 8 085436.
- [90] G. Bimonte, B. Spreng, P. A. Maia Neto, G.-L. Ingold, G. L. Klimchitskaya, V. M. Mostepanenko, R. S. Decca, *Universe* **2021**, 7, 4 93.
- [91] Z. Xu, X. Gao, J. Bang, Z. Jacob, T. Li, *Nature nanotechnology* **2022**, 17, 2 148.
- [92] Z. Xu, P. Ju, X. Gao, K. Shen, Z. Jacob, T. Li, *Nature Communications* **2022**, 13, 1 6148.
- [93] Z. Xu, P. Ju, K. Shen, Y. Jin, Z. Jacob, T. Li, *arXiv preprint arXiv:2403.06051* **2024**.
- [94] A. Roy, U. Mohideen, *Physical review letters* **1999**, 82, 22 4380.
- [95] T. Ederth, *Physical Review A* **2000**, 62, 6 062104.
- [96] L. Zhang, L. You, L. Ying, W. Peng, Z. Wang, *Physica C: Superconductivity and its applications* **2018**, 545 1.
- [97] E. Khestanova, J. Birkbeck, M. Zhu, Y. Cao, G. Yu, D. Ghazaryan, J. Yin, H. Berger, L. Forro, T. Taniguchi, et al., *Nano letters* **2018**, 18, 4 2623.

- [98] S. Schmid, L. G. Villanueva, M. L. Roukes, *Fundamentals of nanomechanical resonators*, volume 49, Springer, **2016**.
- [99] C. Zhang, M. Giroux, T. A. Nour, R. St-Gelais, *Physical Review Applied* **2020**, *14*, 2 024072.
- [100] T. Smith, T. Finlayson, *Journal of Physics F: Metal Physics* **1976**, *6*, 5 709.
- [101] M. Simpson, T. Smith, *J. Low Temp. Phys.:(United States)* **1978**, *32*, 1.
- [102] N. Nelson-Fitzpatrick, C. Guthy, S. Poshtiban, E. Finley, K. D. Harris, B. J. Worfolk, S. Evoy, *Journal of Vacuum Science & Technology A* **2013**, *31*, 2.
- [103] D. Maier-Schneider, J. Maibach, E. Obermeier, *Journal of microelectromechanical systems* **1995**, *4*, 4 238.
- [104] R. W. Revie, *Corrosion and corrosion control: an introduction to corrosion science and engineering*, John Wiley & Sons, **2008**.
- [105] D. C. Mattis, J. Bardeen, *Physical Review* **1958**, *111*, 2 412.
- [106] M. Tinkham, *Introduction to superconductivity*, Courier Corporation, **2004**.
- [107] T. Hong, K. Choi, K. Ik Sim, T. Ha, B. Cheol Park, H. Yamamori, J. Hoon Kim, *Journal of Applied Physics* **2013**, *114*, 24.
- [108] G. Bimonte, H. Haakh, C. Henkel, F. Intravaia, *Journal of Physics A: Mathematical and Theoretical* **2010**, *43*, 14 145304.
- [109] B. Derjaguin, *Kolloid-Zeitschrift* **1934**, *69* 155.
- [110] Y. Zhang, D. Sun, J. Cheng, J. K. H. Tsoi, J. Chen, *Regenerative biomaterials* **2020**, *7*, 1 119.
- [111] R. Behunin, F. Intravaia, D. Dalvit, P. M. Neto, S. Reynaud, *Physical Review A—Atomic, Molecular, and Optical Physics* **2012**, *85*, 1 012504.
- [112] I. Brevik, S. A. Ellingsen, K. A. Milton, *New Journal of Physics* **2006**, *8*, 10 236.
- [113] V. Svetovoy, R. Esquivel, *Journal of physics A: mathematical and general* **2006**, *39*, 21 6777.
- [114] M. Bordag, G. L. Klimchitskaya, U. Mohideen, V. M. Mostepanenko, *Advances in the Casimir effect*, volume 145, OUP Oxford, **2009**.
- [115] V. M. Mostepanenko, *Universe* **2021**, *7*, 4 84.

SUPPLEMENTARY INFORMATION

SUPPLEMENTARY INFORMATION A: PARAMETER TABLE

TABLE S1. Mechanical properties of the NbTiN membranes over small- and big-gaps, and STM setting during the temperature sweep measurements. The length of the device is by design. The gap sizes are measured with a scanning electron microscope (SEM) and with a atomic force microscope (AFM). The tensile stress and the film density of the NbTiN membranes are measured in Supplementary Information **C3**. The thermal expansion coefficients (CTE) of the membranes are fitted from $AT + BT^3$ in the Equation S.33. For membranes suspended over varying gap sizes, distinct AC driving powers yield vibrational amplitudes consistently on the order of tens of picometers.

Parameters	Small gap	Big gap
Length L (um)	709	709
Gap size d (nm)	190	1213
Membrane thickness t (nm)	155	155
Backgate thickness (nm)	155	155
Resonance frequency f (Hz)	352800	343008
Quality factor Q (~ 4.45 K) ($\times 10^3$)	720	200 - 300
Quality factor Q (~ 14.2 K) ($\times 10^3$)	1000	130 - 170
Tensile stress σ (MPa)	677	683
Density ρ (kg/m ³)	4992	5332
Spring constant k_0 (N/m)	1804	1821
CTE-A (1/K ²)	2.001×10^{-10}	4.289×10^{-10}
CTE-B (1/K ⁴)	9.159×10^{-13}	3.181×10^{-13}
T_C (K)	14.195	14.195
AC driving power (dBm)	-85	-40
Tunneling current (pA)	1	1
Bias voltage V_{bias} (mV)	300	300
Backgate voltage V_{bg} (mV)	300+257.2	300+223.6
Averaging time (ms)	200	200

SUPPLEMENTARY INFORMATION B: ON-CHIP CASIMIR CAVITY FABRICATION

Supplementary Information B1: Layered Chip Fabrication Procedure

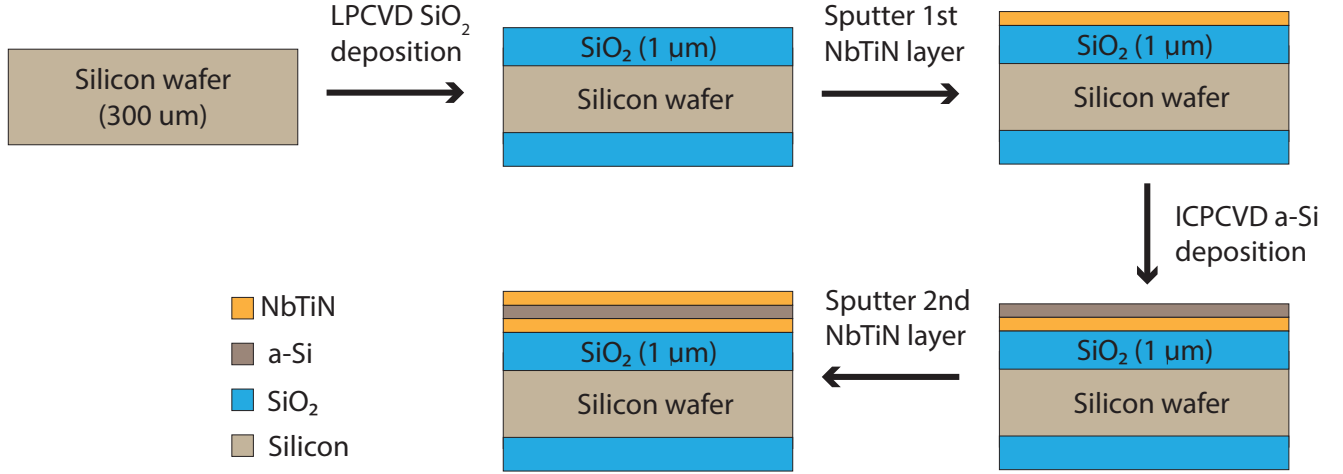


FIG. S6. Fabrication procedure of the layered structure that is later used for fabricating the Casimir cavity.

In this study, the layered chips were fabricated using the following procedure:

1. **Wafer Preparation:** A double-side polished 300 μm bare Si wafer was selected. This thickness was chosen to avoid fragility associated with wafers thinner than 200 μm , while minimizing the measurement uncertainty of thin-film stresses, which increases in wafers thicker than 500 μm .
2. **Insulating Layer Deposition:** A 1 μm thick layer of low pressure chemical vapor deposition (LPCVD) wet thermal oxide (SiO₂) was deposited on the Si wafer to form a robust insulating barrier.
3. **First NbTiN Film Deposition:** A 155 nm layer of niobium titanium nitride (NbTiN) was sputtered onto the SiO₂-coated front side of the wafer using a Sputter system from AJA Int. (SuperAja) at the Kavli Nanolab. Deposition parameters were: Chamber temperature 20 $^{\circ}\text{C}$; Initial chamber pressure lower than 5×10^{-7} mbar; Target composition: NbTi (Nb:Ti=7:3); Deposition time 300 s; Power 250 W; N₂ flow 3.5 sccm; Argon flow 50 sccm; Voltage 300 V; Vacuum level during deposition 2.3 mTorr; Pre-sputtering time 2 min.
4. **Amorphous Silicon Deposition:** An amorphous silicon (a-Si) layer was deposited onto the NbTiN film by Inductively Coupled Plasma Chemical Vapor Deposition (ICP-CVD) using a PlasmaPro 100 system (Oxford Instruments). The deposition conditions were: Temperature 300 $^{\circ}\text{C}$; Plasma power 1000 W; SiH₄ flow 20 sccm; Argon flow 20 sccm; Pressure 10 mTorr.
5. **Second NbTiN Film Deposition:** A second 155 nm NbTiN film was sputtered onto the a-Si layer using the same parameters as described in step 3.
6. **Annealing:** The wafer was annealed on the ICP-CVD table at 300 $^{\circ}\text{C}$ for 20 min in a high-vacuum environment.
7. **Dicing:** Finally, the wafer was coated with dicing resist, spin-coated at 1000 rpm, and baked at 110 $^{\circ}\text{C}$ for 5 min. The processed wafer was subsequently diced into $8 \times 10 \text{ mm}^2$ chips for further processing.

Supplementary Information B2: On-Chip Superconducting Casimir Cavity Fabrication

Following the dicing of the wafers into microchips, the on-chip superconducting Casimir cavity is fabricated using the process outlined below:

1. **Resist Removal:** The dicing resist on each microchip is removed by sequentially rinsing with acetone and isopropanol (IPA).
2. **E-beam Resist Coating:** The microchips are spin-coated with the e-beam resist ARP-6200-13 (CSAR13) at 1300–1500 rpm, followed by a bake at 150 $^{\circ}\text{C}$ for 3 min.
3. **Pattern Writing:** The desired pattern is written on the resist using electron beam lithography.

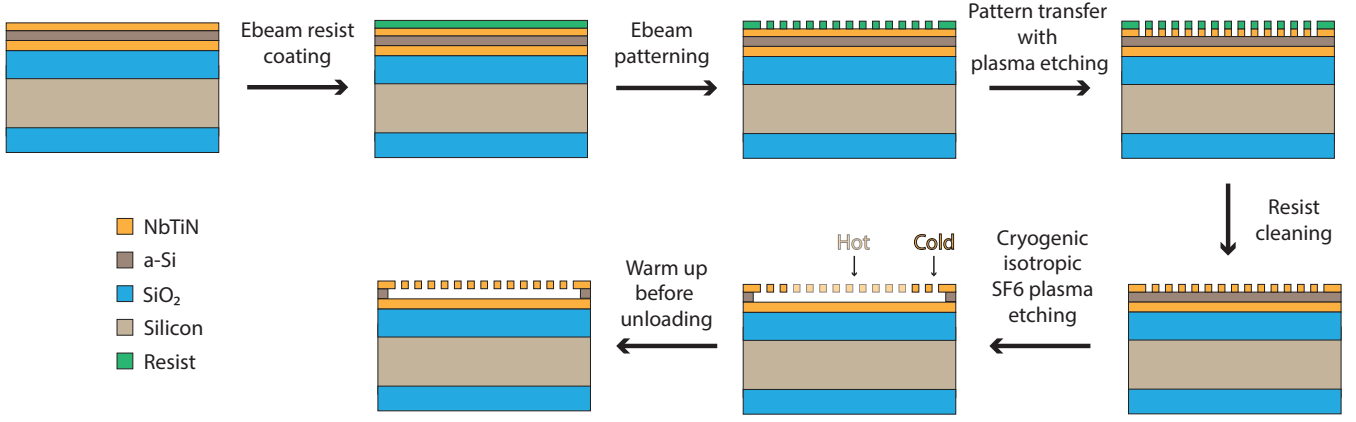


FIG. S7. Fabrication of the superconducting Casimir cavity.

4. **Resist Development:** The e-beam pattern is developed sequentially in the following solutions (each for 1 min): pentyl acetate, a 1:1 mixture of MIBK:IPA, and IPA.
5. **Plasma Etching:** The developed pattern is transferred onto the top NbTiN layer by plasma fluorine etching using CHF_3 (25 sccm) and Ar (25 sccm) at 60 W power, 0.01 mbar pressure, for 45 min. This step was performed using the Sentech F2 system at the Kavli Nanolab Delft.
6. **Resist Removal:** The e-beam resist is removed by first immersing the microchips in a hot Dimethylformamide (DMF) bath (75 °C) for 10 s, followed by a second hot DMF bath (75 °C) in an ultrasonic bath at maximal power (level 9) for 15 min. Residual DMF is subsequently removed by rinsing with acetone and IPA.
7. **Cryogenic SF_6 Undercut:** The final undercut is performed at -120 °C using SF_6 plasma. Prior to etching, the sample is cooled down in a high-vacuum environment with a 10 sccm helium flow for 15 min. The etch is then conducted for 3 min and 10 s with SF_6 plasma, where the RF power is set to 0 W and the ICP power to 3000 W. After etching, the sample is warmed to 40 °C, pumped out, and then unloaded from the process chamber.

Supplementary Information B3: Choice of materials for Casimir cavity

The reasons for choosing niobium titanium (NbTiN) and inductively-coupled-plasma chemical vapor deposition (ICP-CVD) amorphous silicon (a-Si) as the cavity layers are summarized below.

For the bottom layer, one could, in principle, use either a gold film or a superconducting film. However, gold films tend to be relatively inert and adhere strongly to subsequently deposited layers (e.g., plasma-enhanced chemical vapor deposition (PECVD) SiO_2 /a-Si and ICP-CVD a-Si layers). To avoid these issues, we opted for a superconducting film instead. Although aluminum (Al) and NbTiN are both commonly used superconductors, we selected NbTiN for several reasons [14]. First, its high critical temperature (T_C) enhances the sensitivity of the Casimir effect to the superconducting transition. Second, most cryogenic setups with low mechanical vibrations, such as the STM, cannot be cooled below 1 K, making NbTiN an ideal choice for both the bottom and top layers of the superconducting cavity. Lastly, the cryogenic SF_6 dry etching process (performed at -120 °C) exhibits high etch selectivity between NbTiN and a-Si (exceeding 1000), and the small gap configuration ensures that the top NbTiN layer remains well-thermalized (except at the final undercut), allowing the superconducting layers to remain parallel and unetched during the undercutting process.

Compared to other superconducting thin films like Al, the NbTiN film forms only a relatively thin native oxide when exposed to air, unlike the dense 1–3 nm oxide that typically forms on Al surfaces [104]. This native oxide on NbTiN can be removed by annealing at elevated temperatures [96], thereby cleaning the surface prior to STM measurements. Removing the surface oxide is crucial for Casimir force experiments, as residual electrostatic charges on the oxide can limit the measurement resolution.

ICP-CVD a-Si was chosen as the sacrificial layer because it can be undercut using cryogenic SF_6 dry etching. Dry etching is preferred for undercutting small-gap structures since wet etching introduces surface tension effects that limit the aspect ratio of the suspended structure. Although SiO_2 can also serve as a sacrificial layer and be undercut with vapor hydrofluoric acid (HF), we found that vapor HF aggressively attacks NbTiN. Moreover, we opted for ICP-CVD instead of PECVD because PECVD-deposited SiO_2 /a-Si films tend to develop bubbles after the deposition of the top NbTiN layer. These bubbles likely arise from residual hydrogen in the amorphous film, a consequence of using NH_3 during the PECVD process. In contrast, the high plasma power available in ICP-CVD allows the use of N_2 instead of NH_3 during deposition, even at lower temperatures, thereby avoiding bubble formation.

Supplementary Information B4: Microchip Design and Sample Preparation for STM Measurement

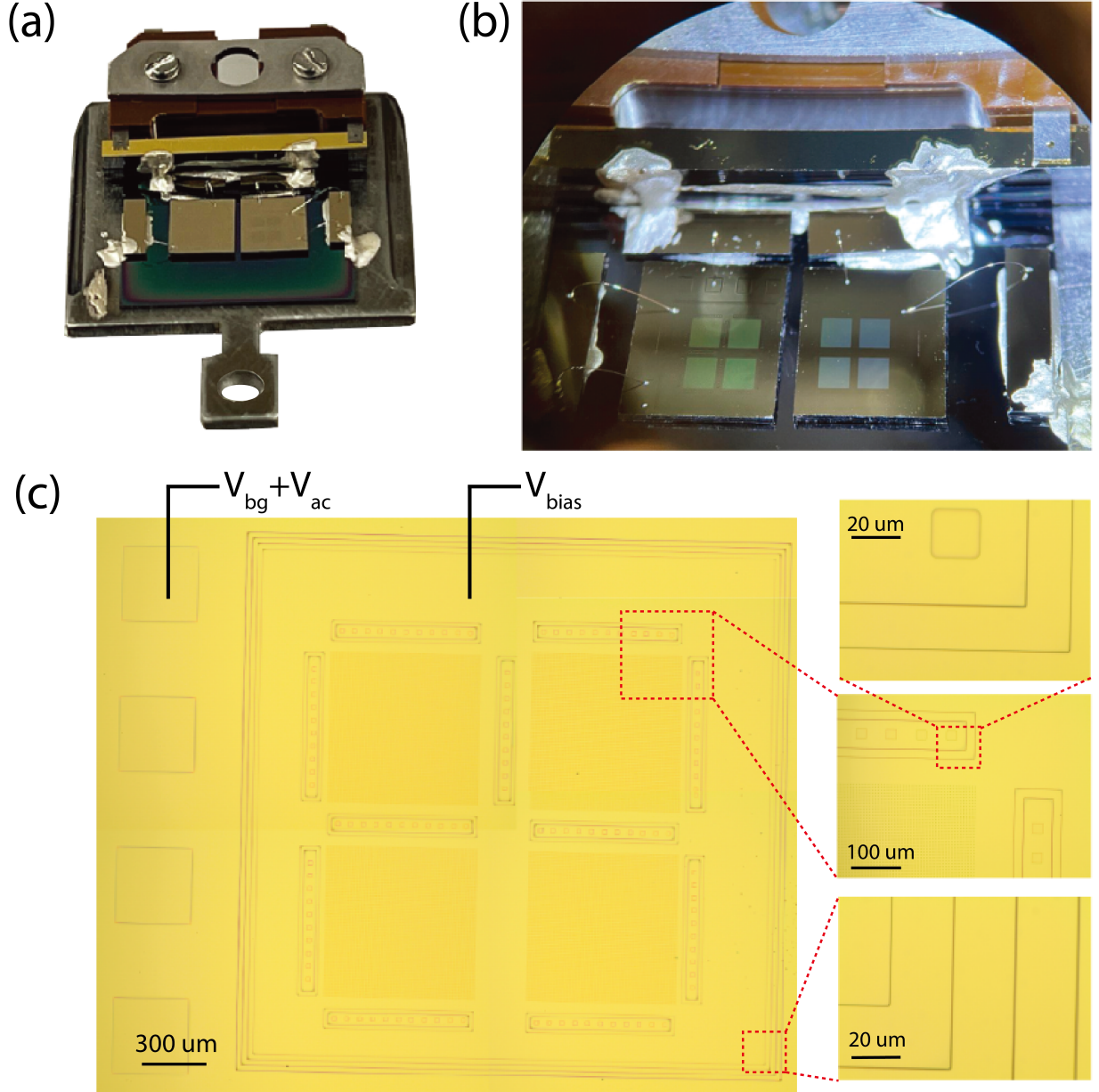


FIG. S8. (a) Photo of the STM holder with small- and big-gaps chips on top. (b) Optical microscope image of the STM holder. (c) Optical images of the small-gap chip, with suspended membranes, electrical isolation patterns, and boxes for accessing electrically to the backgate electrodes.

The microchip used to measure the variation of the Casimir force between superconductors during the phase transition is designed for optimal compatibility with the scanning tunneling microscopy (STM) system. The microchip layout consists of four key components:

1. **Suspended Membranes:** NbTiN membranes are suspended over small gaps by introducing arrays of holes on top, forming the core measurement region.
2. **Recognition Pattern Box:** A reference pattern is incorporated to assist the in-situ STM optical camera in identifying the exact landing position of the STM tip on the microchip. This recognition is facilitated by the bending of relatively large pattern edges after SF_6 undercut etching, which alters the reflection intensity detected by the camera. The objective is to ensure precise STM tip alignment at the very edge of the suspended membrane, minimizing tip-sample interactions during measurement.

3. **Electrical Isolation Rings:** Electrical isolation structures encircle both the suspended membranes and the recognition pattern boxes. These rings prevent unintended electrical shorting between the top and bottom metallic layers. The isolation rings consist of four concentric rings with varying widths, from 50 nm to 200 nm, ensuring that the NbTiN top layer ($t = 155$ nm) is completely etched through while simultaneously restricting the SF_6 undercut size. This design minimizes potential electrical shorting in narrow-gap structures.
4. **Connection Boxes:** Dedicated connection regions facilitate wire bonding between the bottom NbTiN layer and the STM holder, establishing reliable electrical contact.

Following fabrication of the microchip with the superconducting Casimir cavity, the chips are mounted onto the STM holder for integration into the STM system. The preparation steps are as follows:

1. **Electrical Short Testing:** The electrical connectivity between the back gate and the suspended membrane is verified using a probe station at the Kavli Nanolab.
2. **Chip Mounting with Conductive Adhesive:** The chip is affixed to the holder using EPOTEK ELECTRICAL ADHESIVE P.N. H20E (prepared by mixing equal masses of part A and part B). The adhesive is cured by baking at 150°C for 5 min.
3. **STM Holder Assembly:** The holder chip consist of two $1 \times 12\text{ mm}^2$, 1-mm-thick bars (one coated with Au layer on top, the other coated with thick PECVD SiO_2 to achieve electrical isolation), a $12 \times 10\text{ mm}^2$ 300 μm bottom chip (coated with thick PECVD SiO_2), and two $1 \times 5\text{ mm}^2$ 300 μm small pieces. The assembly process involves the following steps: (1) The isolation bar is first glued onto the base chip, followed by the Au-coated bar on top of the isolation bar. This structure is then baked. (2) The assembled dummy chip is glued onto the STM holder, with the four small pieces positioned on the sides and baked again. (3) The small piece chips (two of them) are electrically connected to both the STM holder and the Au-coated bar, as well as to the remaining two small chips using epoxy, followed by another baking step. (4) The electrical probe components are screwed onto the STM holder. Finally, the sample chips are glued onto the dummy chip and baked.
4. **Wire Bonding:** The membranes and back gates of the sample chip are wire bonded to the dummy chip holder, ensuring stable electrical connections.
5. **High-Vacuum Baking:** The STM holder is placed inside the STM load lock and baked at 200°C under high vacuum ($< 10^{-8}$ mbar) for two days. This step removes contaminants such as native oxides and residual organic materials.
6. **STM System Integration and Measurement:** The sample is transferred into the STM head. The STM tip is sharpened using a flat copper sample before commencing measurements.

SUPPLEMENTARY INFORMATION C: ADDITIONAL INFORMATION ON MITIGATING UNWANTED FORCES

Supplementary Information C1: Signature of minimized tip-membrane interaction

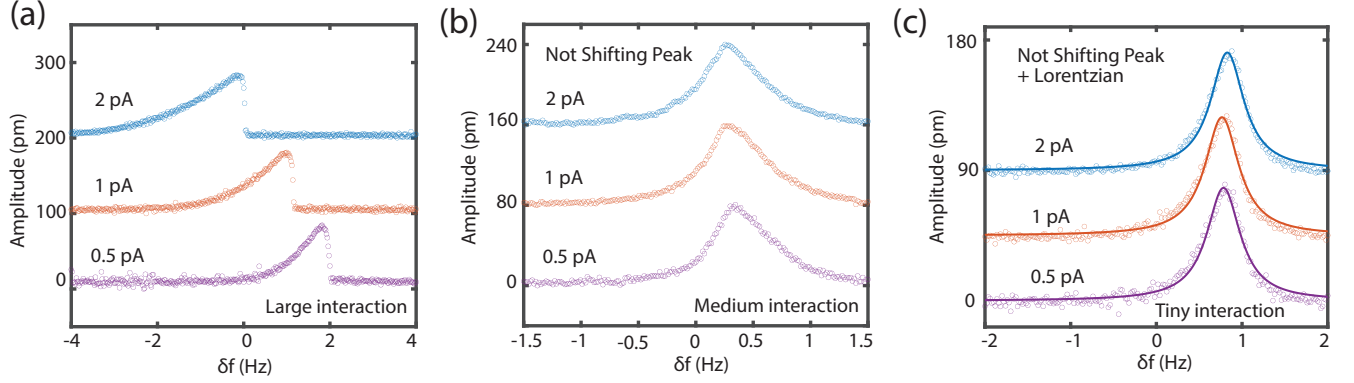


FIG. S9. Confirmation of minimizing the tip-membrane interaction by checking the 1-1 mode peak of the membrane. **(a)** With relatively strong interaction between the tip and the membrane, the peak does not have a Lorentzian shape and shifts as the tunneling current increases. **(b)** With relatively weak interaction between the tip and the membrane, the peak does not have a Lorentzian shape but does not shift as much when the tunneling current increases. **(c)** With minimized interaction between the tip and the membrane, the peak has a Lorentzian shape and does not shift when the tunneling current increases.

Supplementary Information C2: STM tip preparation before measurement

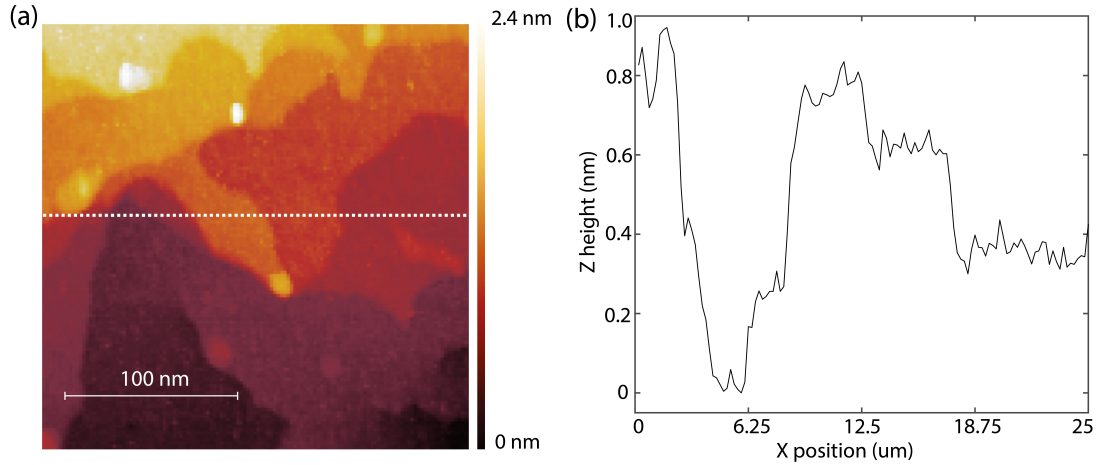


FIG. S10. **(a)** STM scan on an atomically-flat Copper sample. The tip is prepared to be sharp enough, such that **(b)** atomic-scale steps can be observed.

A well-shaped STM tip is essential for atomic-scale imaging and achieving high-resolution data. The fabrication and conditioning process for the STM tip is as follows:

1. **Tip Fabrication and Cleaning:** The STM tip, made of tungsten (W), is fabricated by electrochemically etching tungsten wires in a KOH solution. Once the tip is made and dropped into an in-situ catcher, it is rinsed in distilled water and further cleaned by ultrasonic agitation in isopropanol (IPA) before installation into the tip holder.
2. **Tip Installation and Conditioning:** Following installation, the tip holder undergoes annealing and sputtering in the STM's preparation chamber. The holder is then transferred to the STM measurement stage and is ready for use.

3. **Tip Sharpening on an Atomically Flat Copper Sample:** Prior to measuring the Casimir samples, an atomically flat copper sample is used to pre-condition the STM tip. This involves: (1) Pulsing the tip with appropriate voltages, and (2) Dipping the tip into the copper sample. These steps refine the tip's profile, yielding atomic resolution as confirmed by imaging a step height portfolio on the copper sample, as shown in Fig. S10(b).
4. **Positioning the STM Tip on Casimir Cavities:** The in-situ optical camera is employed for recognition of the membrane's location, then the STM tip can be positioned on the spot, where is approximately $50 \mu\text{m}$ from the edge of the Casimir cavity. This placement minimizes unwanted interactions between the tip and the suspended membrane. Once positioned, the tip is gently dipped into the membrane by approximately 2 nm for a few seconds. This ensures that the measurement spot conforms well to the apex of the tip, facilitating high-resolution scans over a $100 \times 100 \text{ nm}^2$ area. When the STM tip can perform a high-resolution scan over $100 \times 100 \text{ nm}^2$ around a chosen spot, we consider the chosen spot to be stable enough for measurements.
5. **Resonance Measurement and Spot Selection:** Identifying a suitable measurement spot is nontrivial, particularly since the NbTiN surface lacks the flatness of the copper sample. Instabilities and surface imperfections may necessitate the exploration of multiple areas until an ideal spot is found. With a stable measurement spot, resonance peaks of the suspended membrane are determined by sweeping the AC drive signal applied to the bottom NbTiN film. The peaks are verified to exhibit a normal Lorentzian shape, free from nonlinear effects such as hardening or softening, which is critical for confirming the minimization of tip-membrane interaction, thereby preserving the membrane's mechanical quality (Q) factor and enhancing the Casimir force measurement resolution.
6. **Temperature Sweep Considerations:** During measurements of the membrane's resonance frequency as a function of temperature, it is important that the STM tip cannot be retracted out of the tunneling range in the z -direction, since the piezo-actuator's expansion or contraction in the x/y -directions with temperature variations can cause the loss of the original measurement spot. As a result, the atomic tracker, a feedback system in the STM for tracking the same spot on the topography, is activated not only during high-resolution measurement (with a radius of 10 pm) but also during temperature changes (with a tracking radius of approximately 100 pm).

Supplementary Information C3: Film stress measurement based on electrostatic force pulling

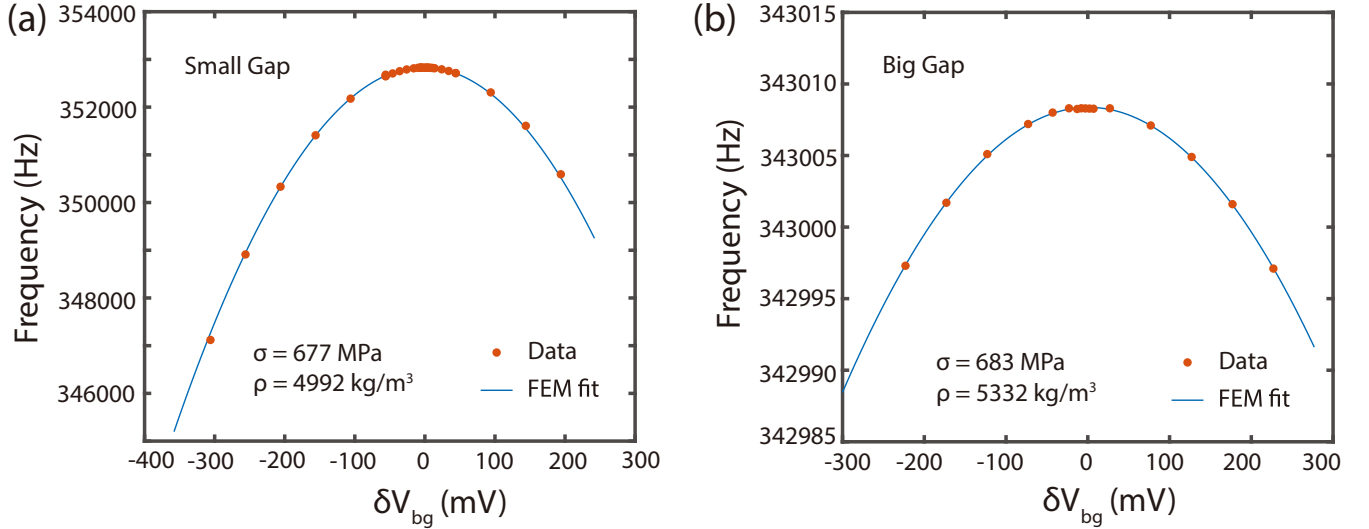


FIG. S11. Local contact potential difference (LCPD) measurements for checking the equilibrium backgate voltages of the membrane over (a) small- and (b) big-gaps. From the experimental results (orange dots), one can fit with the finite element model (FEM) result (blue line), and find the tensile stresses and densities of the membranes. The results obtained from FEM simulation is matching very well with the analytical formula Equation S.16. From the LCPD measurement, film densities and film stresses of NbTiN membranes suspended over small- and big-gap cavities can be calculated.

Local contact potential difference (LCPD) measurements on both small- and large-gap membranes allow us to record resonance frequencies as a function of backgate voltage (V_{bg}). Applying Equation S.16, the angular frequency square shift becomes

$$\Delta\omega^2 = -\frac{\epsilon_0}{\rho t} \frac{(V_{bg} - V_0)^2}{d^3} - \frac{\epsilon_0}{\rho t} \frac{\delta V_{bg}^2}{d^3}, \quad (\text{S.1})$$

where ϵ_0 is the vacuum permittivity, ρ is the film density, t is the membrane thickness, V_{bg} is the backgate voltage, and V_0 is the residual electrostatic voltage. Fitting the experimental data with the above formula, yields the densities (ρ) of the suspended NbTiN membranes, while the peak frequencies of the parabolic response curves provide the film stresses.

Supplementary Information C4: Spectroscopy (I - V) measurement for checking the bias voltage's influence on the membrane frequency

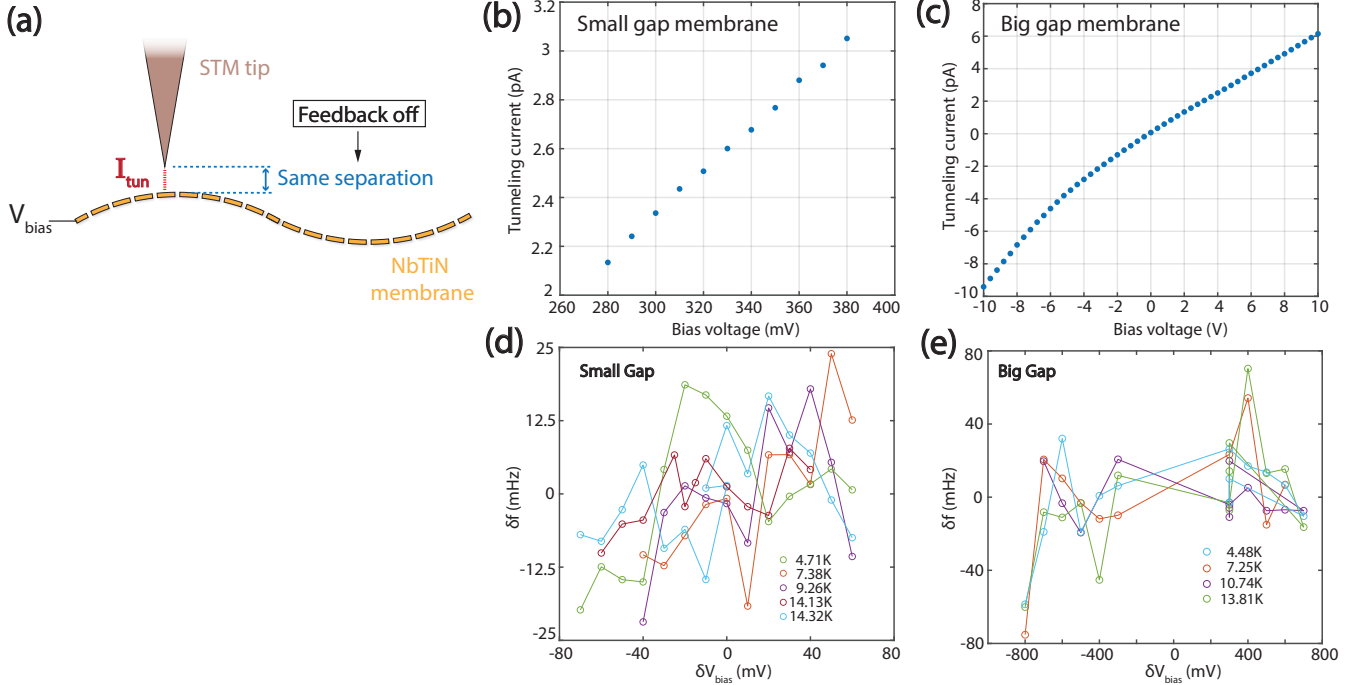


FIG. S12. (a) Schematic of the spectroscopy (I - V) measurement, where the separation between the STM tip and the suspended membrane is kept the same, by varying the bias voltage between the STM and the membrane, and turning off the feedback control of the tunneling current. Tunneling current I as a function of the bias voltage (V), between the STM tip and the (b) small- and (c) big-gap membranes, for each pair of I - V values, the tip-sample separation are kept. These values are used for checking whether the tip-sample interaction depends on the bias voltage, as well as the dependence on the temperature, as shown in (d) for small-gap membrane, and in (e) for big-gap membrane.

Experimental results on the nanomembranes' resonant frequencies dependence on the bias voltage is shown in Fig. 3(d) in the main text. The experiment is performed by setting the separation between the STM tip and the membrane unchanged, and varies the bias voltage and thus the tunneling current between the tip and the membrane. The corresponding tunneling current values at different voltages are shown in Fig. S12(b) for small-gap and (c) for big-gap membranes. The insets in Fig. 3(d) are shown with more details in Fig. S12(d) for small-gap and (e) for big-gap membranes

SUPPLEMENTARY INFORMATION D: MEASUREMENTS WITH ATOMIC FORCE MICROSCOPY

Supplementary Information D1: Roughness and thickness measurement of the NbTiN films

We performed atomic force microscopy (AFM) measurement to identify the roughness of the NbTiN suspended membranes and backgates (bottom films) after the cryogenic SF_6 plasma undercut. In Fig. S13, we show the AFM scan of the backgate films on the small-gap (Panel (a)) and big-gap (Panel (c)) chips, whose RMS roughness are (0.90 ± 0.05) nm and (0.96 ± 0.07) nm, respectively. The area exposed to the plasma etchant is roughened up to (1.73 ± 0.55) nm and (1.78 ± 0.80) nm for the small- and big-gap bottom films, respectively. The zoom-in images of the bottom films under the small- and big-gap cavities, are shown in Panel (b) and Panel (d), respectively, showing the patch sizes of the NbTiN films to be around $\ell = 20 \sim 30$ nm in radius.

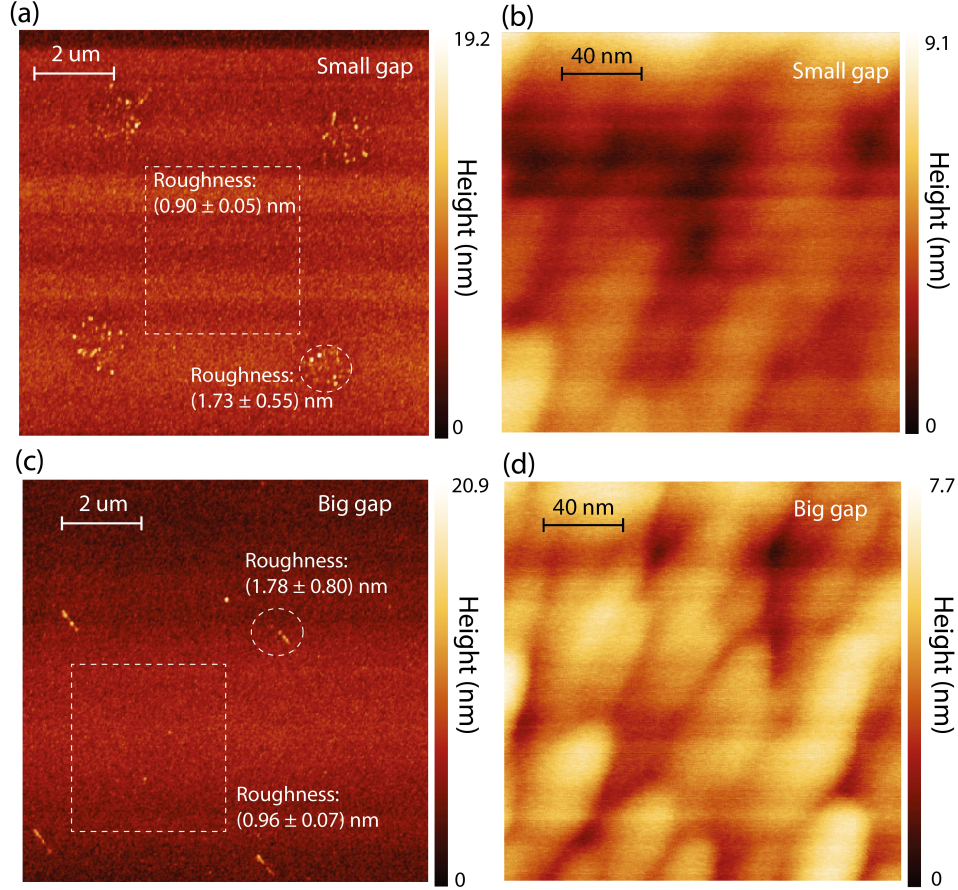


FIG. S13. Atomic force microscope scan on the bottom superconducting films. The Panels (a) and (c) represent the large span topography of the bottom backgate films of the small- and big-gap cavities, respectively. Panels (b) and (d) are topography over a small span, respectively, i.e. the right figures are the zoom-in scans of the figures on the right. From these AFM scans, the patch sizes of the NbTiN films are found to be around $\ell = 20 \sim 30$ nm in radius.

In Fig. S14, we scan the top of the membranes on small- (Panel (a)) and big-gaps (Panel (b)), after they collapsed to the bottom. The roughness of the top membrane over the small-gap cavity is (1.50 ± 0.27) nm, while the one over the big-gap cavity is (2.73 ± 0.26) nm, from which we know that depositing a thicker amorphous silicon layer (1213 nm instead of 190 nm), will increase the roughness of the top NbTiN film a bit.

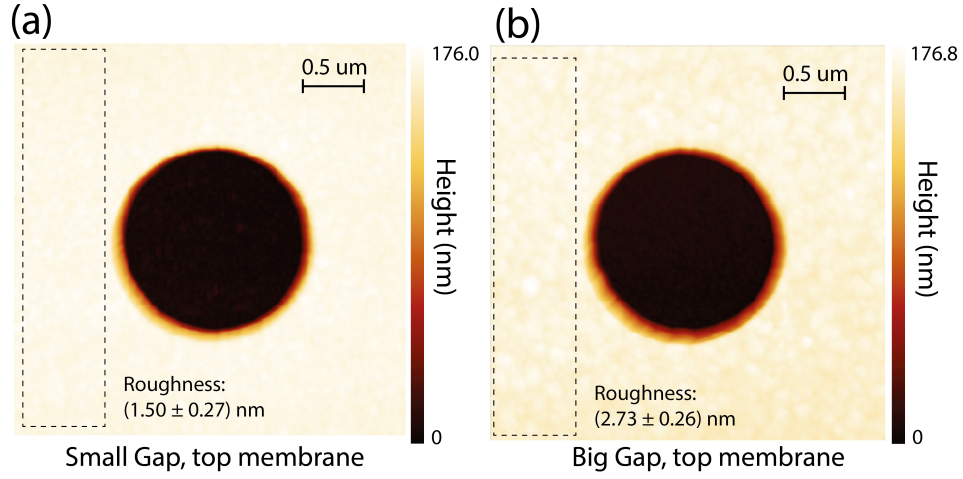


FIG. S14. Atomic force microscope scan on top of the NbTiN membranes after they are collapsed to the bottom film. Panels (a) and (b) represent the topography of the suspended membrane over the small- and big-gap cavities, respectively. The thickness of the membranes are both around 155 nm.

Supplementary Information D2: Gap size measurement of the Casimir cavities

By comparing the heights of the collapsed membranes over the small-gap (Panel (b)) and big-gap (Panel (d)) cavities in Fig. S15, we found both the thicknesses of the membranes over the small- and big-gap to be around 155 nm. From Panels (a) and (c), the small-gap size is found to be $(345-155)=190$ nm, and the big gap size is found to be $(1368-155)=1213$ nm, both matching the values we measured with the SEM. Here the suspended films are fabricated with large opening windows on the top NbTiN films, thus large overhangs are realized and the film stresses are released. for the convenience of AFM scan,

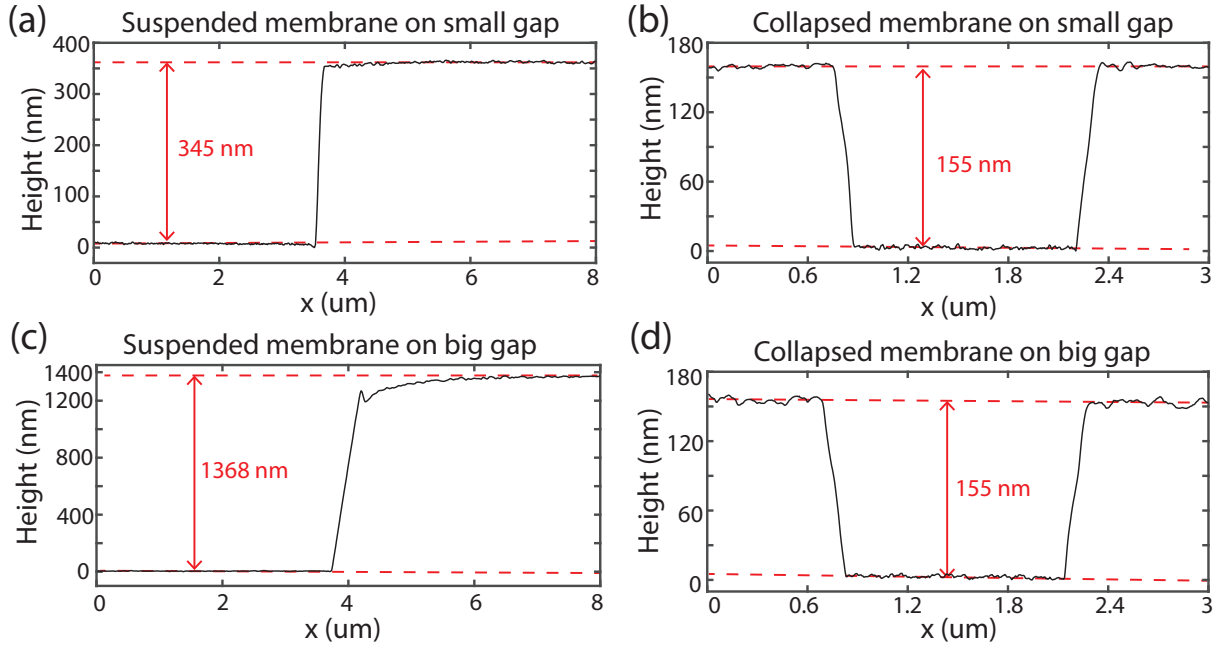


FIG. S15. Atomic force microscope scan on the top NbTiN suspended membranes before, and after (right column) they are collapsed to the bottom film. The top and bottom images represent the topography of the suspended membrane over the small- and big-gap cavities. The thickness of the NbTiN membranes are both found to be around 155 nm for small- and big-gap membranes.

SUPPLEMENTARY INFORMATION E: SCANNING TUNNELING SPECTROSCOPY THE
SUPERCONDUCTING GAP

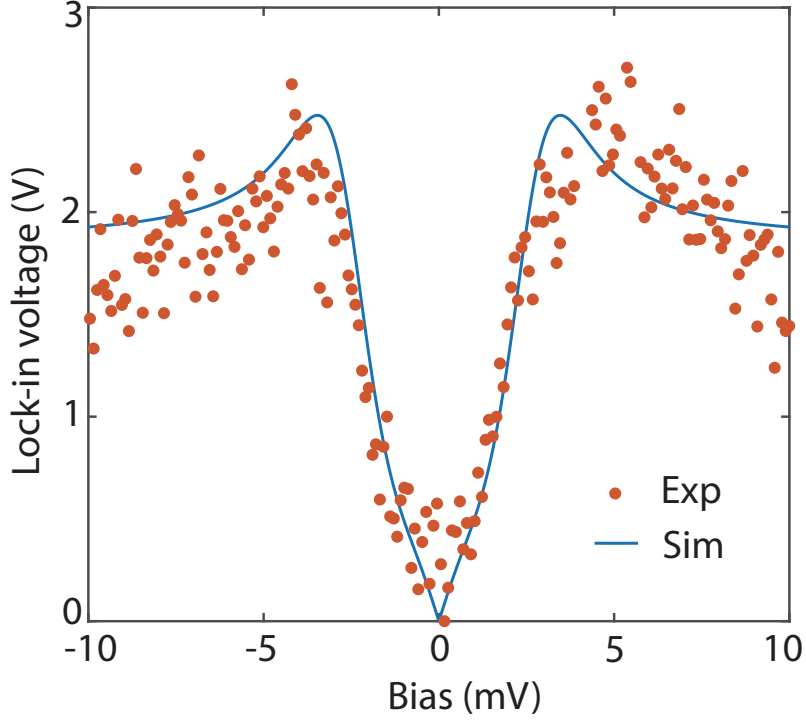


FIG. S16. Scanning Tunneling spectroscopy of the superconducting gap on the suspended membranes over the big gap cavity. The orange dots are experimental data and the blue line is the analytical fit, by using the superconducting gap $\Delta = 2.6$ meV, $\gamma = 0.465$ meV, $T = 4.6$ K and $T_c = 14.2$ K.

Following the superconducting gap calculation in [97], we fitted the measured tunneling conductance $G(V)$ using the standard expression:

$$G(V_{\text{bias}}) = \frac{dI}{dV_{\text{bias}}} = A \int_{-\infty}^{+\infty} N(E, \gamma, \Delta) \frac{\partial f(E + e \cdot V_{\text{bias}}, T)}{\partial (e \cdot V_{\text{bias}})} dE, \quad (\text{S.2})$$

where V_{bias} is the bias voltage, I is the tunneling current, Δ is the superconducting gap, γ is the quasi-particle lifetime broadening (relaxation), N is the density of state (DoS) at the Fermi level for the superconducting electrode, and $f(E + e \cdot V, T)$ is the Fermi-Dirac distribution at temperature T . The superconducting DoS is given by the Dynes formula that applies for thin films

$$N(E, \gamma, \Delta) = \text{Re} \left[\frac{E - i\gamma}{(\sqrt{(E - i\gamma)^2 - \Delta^2})} \right]. \quad (\text{S.3})$$

For the superconducting films used in this paper, the experimental data can be fitted with $\Delta = 2.6$ meV and $\gamma = 0.465$ meV, similar to the values used in Bimonte's work [14].

SUPPLEMENTARY INFORMATION F: THEORETICAL ANALYSIS

Supplementary Information F1. Frequency responses to electrostatic and Casimir forces

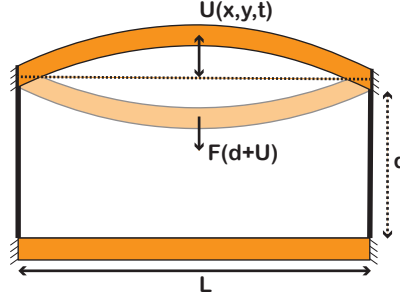


FIG. S17. Schematic of a parallel plate capacitor under an external force.

The resonance frequency of the parallel plate capacitor, consists of a suspended NbTiN membrane under the electrostatic and the Casimir interaction with the fixed NbTiN backgate, is calculation in this Supplementary Information. The schematic of the device is illustrated in Fig. S17. We focus on analyzing the fundamental mode frequency ω_0 (or $\omega_{(1,1)}$). The thin membrane is under high tension, and the height of the membrane is deviated from the equilibrium (not forced) position only by a negligible amount compared to the separation. Based on these considerations, the membrane's dynamics are described by the following equation of motion (EoM) [98]:

$$\rho t \frac{\partial^2 H(x, y; t)}{\partial t^2} - \sigma t \nabla^2 H(x, y; t) = P_{\text{ES}}(H(x, y; t)) + P_{\text{Cas}}(H(x, y; t)) , \quad (\text{S.4})$$

where the height function $H(x, y; t)$ describes the separation between the membrane and the backgate, ρ the density, σ the tensile stress, and t the thickness of the membrane. $P_{\text{ES}}(H(x, y; t))$ and $P_{\text{Cas}}(H(x, y; t))$ are the pressures coming from the electrostatic force and the Casimir force between the membrane and the backgate, respectively. The electrostatic and Casimir forces can be estimated using the additive Derjaguin Proximity Force Approximation (PFA) [109]. This method decomposes the NbTiN surfaces into parallel patch pairs and sums the corresponding pairwise force contributions, thus

$$\rho t \frac{\partial^2 H(x, y; t)}{\partial t^2} - \sigma t \nabla^2 H(x, y; t) = -\frac{\epsilon_0}{2} \left[\frac{(V_{\text{bg}} - V_0)^2}{H^2(x, y; t)} + \frac{V_{\text{rms}}^2(H^2(x, y; t))}{H^2(x, y; t)} \right] + P_{\text{Cas}}(H(x, y; t)) . \quad (\text{S.5})$$

where ϵ_0 is the permittivity of vacuum, V_{bg} is the backgate voltage, V_0 is the residual electrostatic potential, V_{rms} accounts for the force originated by the patches that are smaller than the separation between the plates [11]. By decomposing $H(x, y; t)$ as $d + U(x, y; t)$, where d is the initial separation between the plates, $U(x, y; t)$ is the displacement under the external force, and noting that $|U(x, y; t)| \ll d$. We perform a first-order Taylor expansion of the (unit-area) forces on the right-hand side of the preceding equation, yielding:

$$\rho t \frac{\partial^2 U(x, y; t)}{\partial t^2} - \sigma t \nabla^2 U(x, y; t) - k_{\text{eff}}^2 U(x, y; t) = -\frac{\epsilon_0}{2} \left[\frac{(V_{\text{bg}} - V_0)^2}{d^2} + \frac{V_{\text{rms}}^2(d)}{d^2} \right] + P_{\text{Cas}}(d) , \quad (\text{S.6})$$

where the effective spring constant

$$k_{\text{eff}}^2 = \epsilon_0 \left[\frac{(V_{\text{bg}} - V_0)^2}{d^3} + \frac{V_{\text{rms}}^2}{d^3} - \frac{1}{2d^2} \frac{\partial V_{\text{rms}}^2}{\partial d} \right] + P'_{\text{Cas}}(d) . \quad (\text{S.7})$$

The displacement $U(x, y; t)$ can be further decomposed into $U_0(x, y) + U_f(x, y; t)$, where $U_0(x, y)$ is the static displacement, and $U_f(x, y; t)$ is the time-dependent membrane displacement under the external force. In the case, the membrane is only statically pulled down ($U_f(x, y; t) = 0$), the Equation S.6 can be simplified into

$$-\sigma t \nabla^2 U_0(x, y) - k_{\text{eff}}^2 U_0(x, y) + \frac{\epsilon_0}{2} \left[\frac{(V_{\text{bg}} - V_0)^2}{d^2} + \frac{V_{\text{rms}}^2(d)}{d^2} \right] - P_{\text{Cas}}(d) = 0 , \quad (\text{S.8})$$

implying that the static terms in the force only cause static deflection. Meanwhile, if $U_f(x, y; t) \neq 0$, the Equation S.6 can be written as

$$\rho t \frac{\partial^2 U_f(x, y; t)}{\partial t^2} - \sigma t \nabla^2 (U_0(x, y) + U_f(x, y; t)) - k_{\text{eff}}^2 (U_0(x, y) + U_f(x, y; t)) + \frac{\epsilon_0}{2} \left[\frac{(V_{\text{bg}} - V_0)^2}{d^2} + \frac{V_{\text{rms}}^2(d)}{d^2} \right] - P_{\text{Cas}}(d) = 0 . \quad (\text{S.9})$$

By putting together Equations S.8 and S.9, the EoM is reduced into

$$\rho t \frac{\partial^2 U_f(x, y; t)}{\partial t^2} - \sigma t \nabla^2 U_f(x, y; t) - k_{\text{eff}}^2 U_f(x, y; t) = 0 . \quad (\text{S.10})$$

As shown in [98], $U_f(x, y; t)$ can be written in the form:

$$U(x, y, t) = \sum_{n=1}^{\infty} \sum_{j=1}^{\infty} u_{0,n,j} \phi_{n,j}(x, y) e^{i\omega_{n,j}t}, \quad (\text{S.11})$$

where $\phi_{n,j}(x, y) = \sin \frac{n\pi x}{L_x} \sin \frac{j\pi y}{L_y}$ are the normalized modeshape function, $u_{0,j}$ are the coefficients that weight how much mode (n, j) contributes to the overall vibration, and $\omega_{n,j}$ is the eigenfrequency of the spatial mode $\phi_{n,j}$. The fundamental mode EoM of Equation S.10 can then be obtained by multiplying $\phi_{1,1}$ and integrating over the entire membrane area $A = L \times L$ with $L_x = L_y = L$, following the Galerkin's method, and gives

$$\iint_A \left(\rho t \frac{\partial^2 U_f(x, y; t)}{\partial t^2} - \sigma t \nabla^2 U_f(x, y; t) - k_{\text{eff}}^2 U_f(x, y; t) \right) \phi_{1,1} dx dy = 0, \quad (\text{S.12})$$

then the equation can be written as

$$-\rho t \omega_0^2 \iint_A \phi_{1,1}^2 dx dy + 2 \frac{\pi^2}{L^2} \sigma t \iint_A \phi_{1,1}^2 dx dy - k_{\text{eff}}^2 \iint_A \phi_{1,1}^2 dx dy = 0. \quad (\text{S.13})$$

The EoM results in

$$\omega_0^2 = 2 \frac{\pi^2}{L^2} \frac{\sigma}{\rho} - \frac{k_{\text{eff}}^2}{\rho t}. \quad (\text{S.14})$$

When $k_{\text{eff}} = 0$, the natural eigenfrequency is $\omega_n = \frac{\sqrt{2}\pi}{L} \sqrt{\frac{\sigma}{\rho}}$, and the membrane frequency under a voltage is written as

$$\omega_0^2 = \omega_n^2 \left(1 - \frac{L^2 k_{\text{eff}}^2}{2\pi^2 \sigma t} \right). \quad (\text{S.15})$$

For clarity, we denote temperature-dependent variations in frequencies, pressures, and similar parameters by Δ , while δ indicates changes at a fixed temperature T . From Equation S.14, we can calculate the membrane's frequency response under a given external force to be

$$\delta \omega^2 = \omega_0^2 - \omega_n^2 = -\frac{k_{\text{eff}}^2}{\rho t}, \quad (\text{S.16})$$

or more intuitively, since the effective spring constant equals to the gradient of the external pressure, i.e. $k_{\text{eff}}^2 = P'_{\text{ext}}$, when the membrane is under a separation-dependent external pressure P_{ext} or force F_{ext} , the frequency shift is

$$\delta \omega^2 = -\frac{1}{\rho t} P'_{\text{ext}}(d) = -\frac{1}{\rho t L^2} F'_{\text{ext}}(d), \quad (\text{S.17})$$

implying that the change in ω^2 , is proportional to the pressure (or force) gradient.

While sweeping the temperature of the membrane from T_1 to T_2 , the variation of the external force gradient on the membrane, after calibrating out the frequency shift due to thermal expansion (contraction), is

$$\Delta \omega^2(T_1, T_2) = \delta \omega^2(T_2) - \delta \omega^2(T_1) = -\frac{1}{\rho t L^2} (F'_{\text{ext}}(T_2) - F'_{\text{ext}}(T_1)) = -\frac{1}{\rho t L^2} \Delta F'_{\text{ext}}. \quad (\text{S.18})$$

In our experiment, the electrostatic force is canceled out in the experiment, i.e. $V_{bg} - V_0 = 0$. Meanwhile, the effect of V_{res} , originated from the patches with the average size ℓ ($\ell \ll d$), can be estimated by the pressure of the form $P_{\text{patch}} \approx 0.9 \cdot \epsilon_0 V_{\text{rms}}^2 \ell^2 / d^4$, as shown in [111]. In our case, $\ell \approx 30$ nm is measured via the AFM scan, and reasonably assuming that V_{rms} is less than 10 mV, we have $P_{\text{patch}} < 5.5 \times 10^{-4}$ Pa, which is much smaller than the estimated Casimir pressure $P_{\text{Cas}} \approx -0.4021$ Pa, as estimated in Supplementary Information **H**, thus the pressure contribution from V_{rms} can be safely neglected. Given the above analysis, the effective spring constant $k_{\text{eff}}^2 = P'_{\text{Cas}}(d)$, indicating that the small-gap membrane frequency shift in our experiment, after calibrating out the elastic force dependence on temperature, is a result of the variation in Casimir pressure. In this case, Equation S.15 can be rewritten for $\omega_n - \omega_0 \ll \omega_n$, as

$$\frac{\delta \omega}{\omega_0} = \frac{\delta f}{f} \approx -\frac{L^2}{4\pi^2 \sigma t} P'_{\text{Cas}} = -\frac{1}{4\pi^2 \sigma t} F'_{\text{Cas}}. \quad (\text{S.19})$$

While checking the frequency shift induced by the temperature dependence on the Casimir force, the above equation can be rewritten as

$$\frac{\Delta f}{f} = \frac{\delta f(T_2) - \delta f(T_1)}{f} = \frac{1}{4\pi^2 \sigma t} (F'_{\text{Cas}}(T_2) - F'_{\text{Cas}}(T_1)), \quad (\text{S.20})$$

indicating that the larger the temperature variation of the Casimir force gradient is, the higher percentage of the membrane frequency will shift. When the absolute Casimir gradient has a larger value, the temperature-induced influence on it will be greater, thus the frequency response will be more announced.

Moreover, the frequency response of a parallel plate capacitor, when it is under a generalized force of the form

$$F(d) = \frac{B \cdot A}{(d + U(x, y; t))^n}, \quad (\text{S.21})$$

where B is a separation independent constant, $A = L \times L$ is the surface area of the square membrane, $n > 0$ is the power law factor, and d is the separation. Assuming the membrane is deflecting only slightly, following the calculation procedure presented above, the frequency shift of the membrane under the external force will become

$$\omega_0^2 = 2 \frac{\pi^2}{L^2} \frac{\sigma}{\rho} + \frac{B \cdot n}{\rho t d^{n+1}}, \quad (\text{S.22})$$

and the variation of ω^2 is proportional to the gradients of the external force $F'(d)$ and pressure $P'(d)$:

$$\delta\omega_0^2 = -\frac{P'(d)}{\rho t} = -\frac{F'(d)}{\rho t L^2}. \quad (\text{S.23})$$

Supplementary Information F2: Modifications from the holes on the membranes

For the purpose of releasing the nanomembranes, patterned holes on the membranes are required. By performing finite element method (FEM) simulation, we show the relationships of responses between the nanomembranes with holes and without holes here.

For membranes simulated with identical parameters including lateral size, thickness, Young's modulus, Poisson ratio, tensile stress, and gap size, their responses towards external forces are shown with the subscript 'h' (with holes) and 'nh' (without holes):

$$\left(\frac{f_h}{f_{nh}}\right)^2 = \frac{z_{nh}}{z_h} = \left(\frac{\delta f_{nh}}{\delta f_h}\right)^2 = Y_{\text{ratio}}, \quad (\text{S.24})$$

where $f_\theta = \omega/(2\pi)$ is the linear resonant frequency, z_θ is the center displacement due to the external force, δf_θ is the variation in the linear frequency ($\theta = h, nh$), and Y_{ratio} is the hole-dependent ratio. In our case, the radius of the holes is $0.75 \mu\text{m}$ and the center-to-center separation is $5.5 \mu\text{m}$, $Y_{\text{ratio}} = 0.923$ is obtained from finite element method (FEM) simulation.

As for the change in the angular resonant frequency ω , it is found that

$$\delta\omega_h^2 = \delta\omega_{nh}^2. \quad (\text{S.25})$$

As for the electrostatic and Casimir pressures acting on the membrane, the relation between the membranes with holes and without holes, in our case, is found to be

$$\frac{\text{Membrane area} - \text{Hole area}}{\text{Membrane area}} = \frac{\delta F_h}{\delta F_{nh}} \approx 0.945. \quad (\text{S.26})$$

With FEM simulation, we also confirm that the effective mass of our squared membranes with holes, is still $m_{\text{eff}} \approx 0.25m_0$, where m_0 is the total mass of the membranes after subtracting the masses of holes.

The above relationships are taken into account while analyzing the experimental data.

Supplementary Information F3: Thermal expansion of the nanomembranes

In order to find out the thermal expansion coefficients of the nanomembranes suspended over the small- and big-gap cavity, as shown in Fig. 5(f) in the main text, we derive the membrane frequency dependence on the temperature here. For squared tensile nanomembranes, the linear resonant frequency $f = \omega/(2\pi)$ of the fundamental mode during the temperature (T) sweep is

$$f(T) = \frac{1}{\sqrt{2}L} \sqrt{\frac{\sigma(T)}{\rho}}, \quad (\text{S.27})$$

where $\sigma(T)$ is the temperature-dependent film stress, ρ is the film density, and L is the length of the membrane. We assume that the temperature variation is small $T = T_0 + \Delta T$, where T_0 is the base temperature and ΔT is the temperature variation, this temperature change will lead to a change in stress $\sigma = \sigma_0 + \Delta\sigma$, where $\Delta\sigma$ can be written as [99]

$$\Delta\sigma = -\frac{E}{1-\nu} \cdot \alpha(T) \cdot \Delta T, \quad (\text{S.28})$$

where E is the Young's modulus, ν is the Poisson ratio of the membrane, and $\alpha(T)$ is the temperature-dependent thermal expansion coefficient of the membrane. With this and by using the Taylor expansion, the above equation can be rewritten as

$$f(T) = \frac{1}{\sqrt{2}L} \sqrt{\frac{\sigma_0}{\rho}} \cdot \sqrt{1 + \frac{\Delta\sigma}{\sigma}} = f_0 + \frac{f_0}{2} \frac{\Delta\sigma}{\sigma_0}, \quad (\text{S.29})$$

where $f_0 \approx \frac{1}{\sqrt{2L}} \sqrt{\sigma_0/\rho}$, and the change in frequency becomes

$$\Delta f = f - f_0 = \frac{-f_0}{2\sigma_0} \cdot \frac{E \cdot \alpha(T)}{1 - \nu} \Delta T. \quad (\text{S.30})$$

Since $\sigma_0 = 2L^2 f_0^2 \rho$, the frequency variation becomes

$$\Delta f = \frac{-\alpha(T) \cdot E}{4L^2 f_0 \cdot \rho \cdot (1 - \nu)} \Delta T, \quad (\text{S.31})$$

when the change of the temperature is very small, then $f_0 \rightarrow f(T)$, and the above equation can be written as

$$\Delta f^2 = \frac{-\alpha(T) \cdot E}{2L^2 \cdot \rho \cdot (1 - \nu)} \Delta T, \quad (\text{S.32})$$

From previous studies, the thermal expansion coefficient of superconductors at cryogenic temperature are usually formulated as [100, 101]

$$\alpha(T) = A \cdot T + B \cdot T^3, \quad (\text{S.33})$$

where A and B are the temperature-independent coefficients. The the stress coming from the thermal expansion of the material becomes [102]

$$\sigma_{th} = \frac{E_{film}}{1 - \nu_{film}} \int_{T_1}^{T_2} (\alpha_{film}(T) - \alpha_{sub}(T)) dT, \quad (\text{S.34})$$

where E_{film} and ν_{film} are the Young's modulus and Poisson ratio of the thin film. From [110], we have $E_{film} = 375$ GPa and $\nu_{film} = 0.2949$, α_{film} and α_{sub} are the temperature-dependent thermal expansion coefficient of the thin film and the deposited substrate, respectively.

With the temperature data points shown in Fig. 5(f) in the main text, one can calculate the thermal expansion coefficients of membranes suspending over the small- and big-gap cavities using Equation S.33. For the small-gap membrane

$$\alpha_{sg}(T) = (2.001 \times 10^{-10}) \cdot T + (9.159 \times 10^{-13}) \cdot T^3 \text{ [K}^{-1}\text{]}, \quad (\text{S.35})$$

and for the big-gap membrane

$$\alpha_{bg}(T) = (4.289 \times 10^{-10}) \cdot T + (3.181 \times 10^{-13}) \cdot T^3 \text{ [K}^{-1}\text{]}. \quad (\text{S.36})$$

At $T = 14.2$ K, $\alpha_{sg} = 5.46 \times 10^{-9} \text{ K}^{-1}$ and $\alpha_{bg} = 7.00 \times 10^{-9} \text{ K}^{-1}$. The difference in the thermal expansion coefficients between the two membranes over different gap sizes, can come from the different substrates the two membranes are deposited on, i.e. the different amorphous silicon sacrificial layer thicknesses, which can contribute to the overall membrane frequency dependence on the temperature.

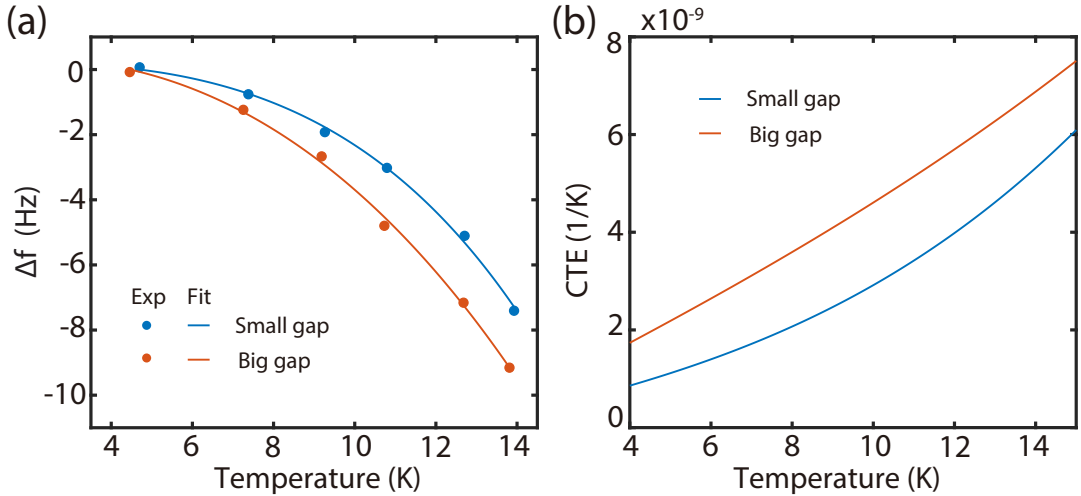


FIG. S18. Thermal expansion coefficient (CTE) of NbTiN membranes. (a) Frequency dependence on temperature for NbTiN membranes suspended over the small- (blue) and big-gap (orange). The dots are experimental data, and the solid lines are the fitting curve. (b) Fitted CTE of NbTiN membranes suspended over the small- (blue) and big-gap (orange). The membranes suspended over cavities of different gap sizes have different CTE, due to the different thicknesses of the amorphous silicon (a-Si) sacrificial layer.

SUPPLEMENTARY INFORMATION G: PROCEDURE ON CALCULATING THE PRESSURE AND FORCE VARIATIONS FROM EXPERIMENTAL FREQUENCY SHIFTS

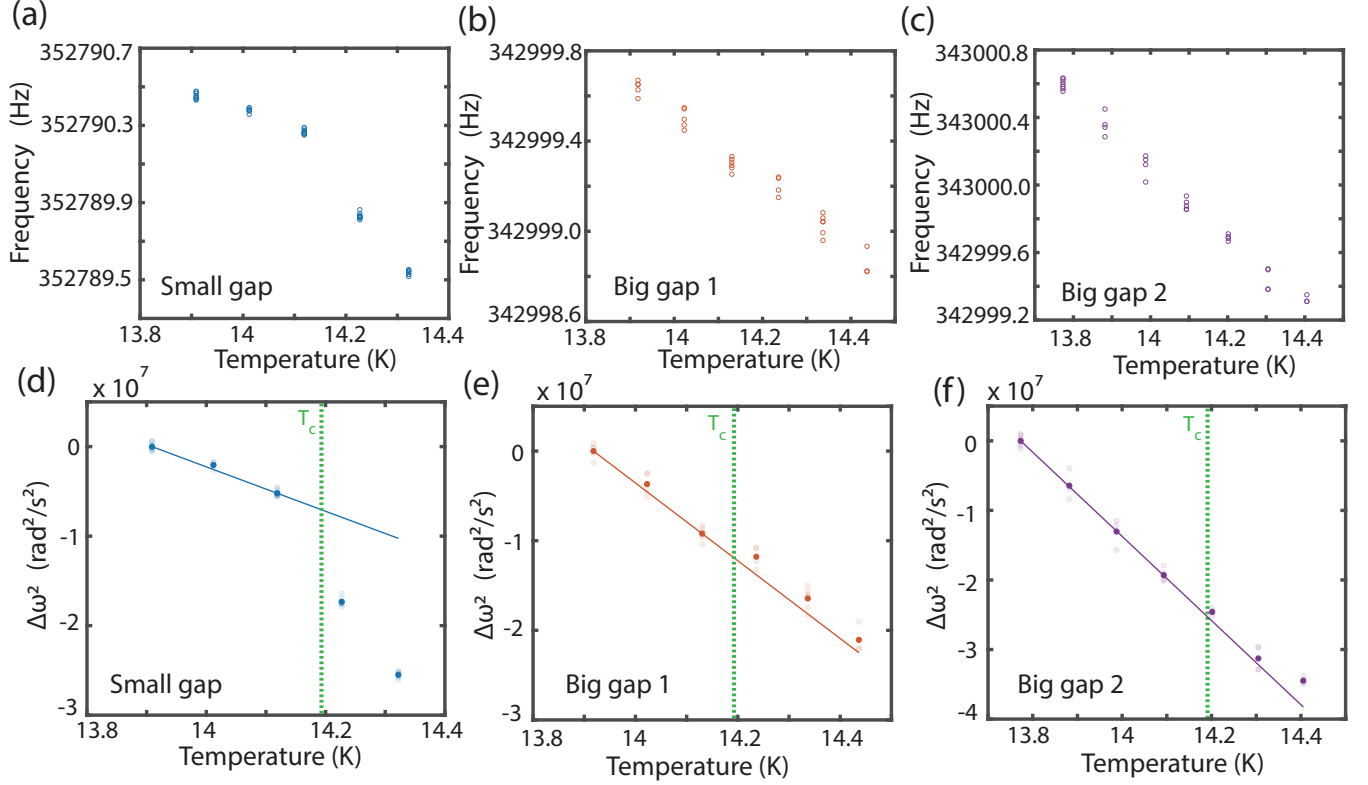


FIG. S19. Calibration of the temperature dependence of the elastic force near T_C . (a) Small-gap membrane, (b) and (c) big-gap membranes resonant frequencies (f) as a function of temperature. After converting the linear frequency to angular frequency ω , we show the variation in ω^2 as a function as temperature in (d) for small-gap membrane, and in (e) and (f) for big-gap membranes. Linear fits are performed on the variation of ω^2 for the small-gap and big-gap membranes, with the aim of calibrating out the thermal expansions of the membranes.

In this paper, the nanomembrane suspended over a 190 nm gap size experiences a variation of resonant frequency that is different from the variation of the big-gap membrane, in order to find the corresponding abrupt pressure/force change on the small-gap membrane near T_C , we first perform linear fits on temperature-dependent frequency data points ($\omega = 2\pi f$) below T_C for both small-gap membrane (Fig. S19d) and big-gap membranes (Fig. S20e) and Fig. S20f), in order to accurately cancel out the thermal expansion of the membranes. Linear fits are used, because for such small temperature span the thermal expansion coefficients can be approximated as constant values. Then we subtract the different between the frequency square values ω^2 at a temperature above T_C from the linear fit, and obtain the variation of angular frequency square $\Delta\omega^2$ for membranes on both gap sizes, which is shown in Fig. S20(a). Later we compare the $\Delta\omega^2$ difference between the two membranes, and use Equation S.17 to check the corresponding force gradient and pressure gradient variations, as shown in Fig. S20(b) and S20(c), respectively, without knowing the exactly behaviors of the external pressure/force. The error bars in Fig. S20(a) are obtained with the different frequency sweep data points for every temperature setting, while the error bars in Fig. S20(b) and S20(c) are calculated by adding up the error bars of $\Delta\omega^2$ for small- and big-gap membranes shown in Fig. S20(a). Here we combined the datasets from the big-gap membranes into one dataset. The error bars of the $\Delta\omega^2$ data on membranes over both gap sizes are obtained from the frequency sweep datasets at each temperature data point, and the error bars of the force gradient and pressure gradient variations are calculated by adding up the error bar size of the small-gap membrane at a certain temperature and the two error bar sizes of the big-gap membrane around the corresponding temperature.

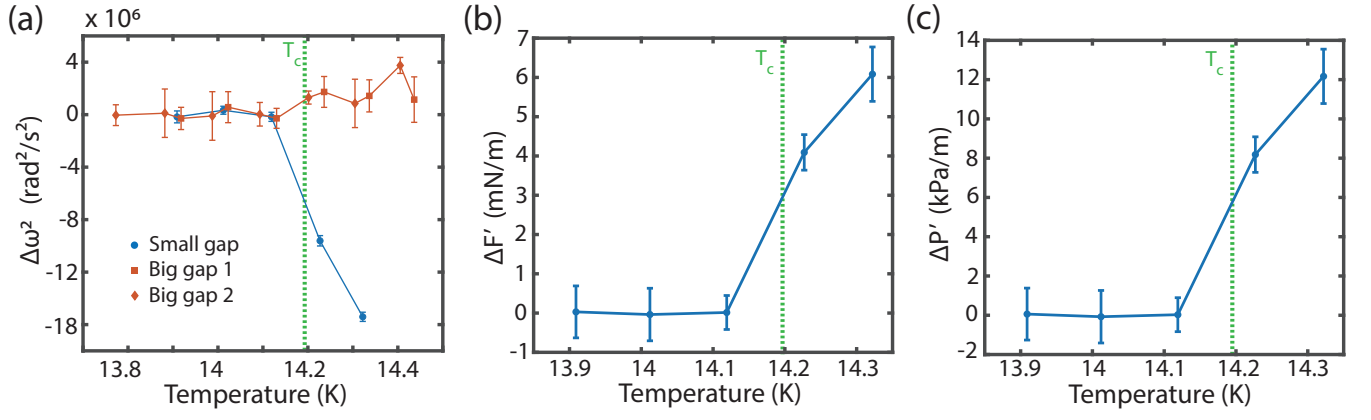


FIG. S20. Procedure on calculating the pressure and force variations from experimental frequency shifts. After performing linear fits on the variation of ω^2 for the small-gap and big-gap membranes, the derivations of ω^2 from the linear fits are shown in Panel (a) for small- and big-gap membranes, where the two big-gap membrane datasets are combine. After subtracting the difference in ω^2 between small- and big-gap membranes, we used Equation S.17 to obtain the corresponding force gradient and pressure gradient variations, as shown in Panels (b) and (c). Here the exact form of the external force/pressure is not required to be known beforehand for the calculation.

SUPPLEMENTARY INFORMATION H: COMPUTING THE CASIMIR PRESSURE BETWEEN SUPERCONDUCTORS AND EXPLAINING ITS ABRUPT CHANGE ACROSS T_C

The most striking finding of our experiment is the abrupt change in the membrane resonance frequency observed across the superconducting transition T_C , as displayed in Fig. S24. This shift corresponds to a sudden increase of approximately 12 kPa/m in the pressure gradient acting on the membrane, as its temperature is raised through T_C . The central question is to elucidate the physical cause of this unexpected result. Strong evidence that the thermal Casimir effect is responsible comes from the observation that the measured increase in the pressure gradient is of the same order of magnitude as the classical Casimir pressure gradient between two conducting plates at distance d :

$$P'_{cl} = \frac{3k_B T}{8\pi d^4} \zeta(3), \quad (\text{S.37})$$

where $\zeta(3) = 1.202$ is Riemann's zeta function. Indeed, at $T = T_C$ and for a separation of $d = 190$ nm, the classical Casimir pressure gradient P'_{cl} is calculated to be 21.6 kPa/m, approximately double the measured increase.

In this Section, we present the theory of the Casimir effect for superconductors, based on the general Lifshitz theory and the BCS theory, which describes their optical properties. It is important to note that precision room-temperature Casimir experiments with metallic test bodies over the last 20 years have shown that computing the classical contribution to the Casimir force is a complex matter. It has been realized that the straightforward approach based on the over 100-year-old Drude model for a metal's conductivity, leading to Equation (S.37), is inconsistent with experimental data. Excellent agreement, however, is achieved when the classical term is computed by modeling a metal as a dissipationless electron plasma. The situation with superconductors remains largely unknown, as no prior experiments have successfully provided information on the influence of the superconducting transition on the Casimir force. We will use our experimental data to guide the development of a theory capable of reproducing our observations. Our analysis indicates that the most promising theoretical framework employs the plasma approach for $T > T_C$ and the BCS theory for $T < T_C$. This approach provides a qualitative explanation for the observed discontinuity in the pressure gradient and, with an appropriate choice of the plasma frequency Ω , can reproduce the observed magnitude of the discontinuity.

Supplementary Information H1: Lifshitz formula for superconductors

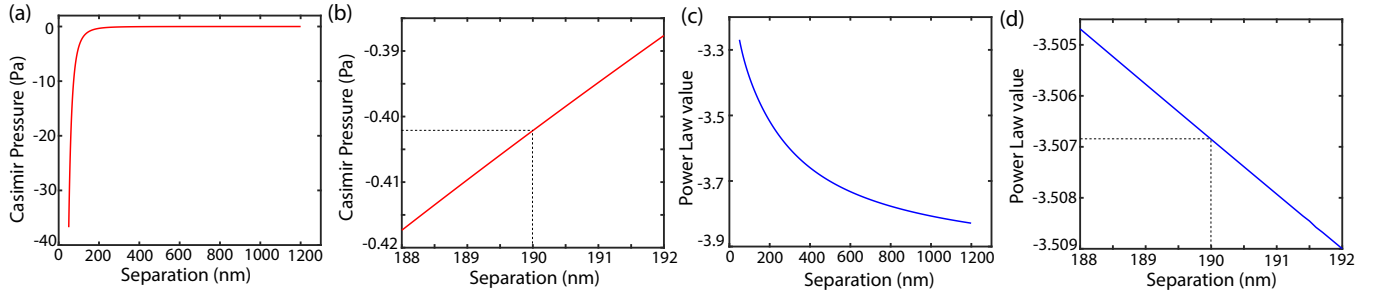


FIG. S21. Estimation of the Casimir pressure between superconductors, at the temperature of $T = 0.99 \cdot T_C$. **(a)** Casimir pressure between superconducting NbTiN surfaces. **(b)** Power law value x in the Casimir pressure $P(d) \sim 1/d^n$ between superconducting NbTiN surfaces. **(c)** Casimir pressure between superconducting NbTiN surfaces, with a separation around 190 nm. **(d)** Power law value x in the Casimir pressure $P(d) \sim 1/d^n$ between superconducting NbTiN around T_C , around 190 nm separation. At 190 nm, the absolute Casimir pressure between NbTiN near T_C , is $P = -0.4021$ Pa, and the power law value is $n = 3.5069$, leading to the explicit expression of the Casimir pressure to be $P_{Cas}|_{d=190\text{nm}} = (-1.081 \times 10^{-24})/d^{3.507}$ [Pa].

We now calculate the Casimir pressure between superconducting surfaces. It is observed that the considerable thickness ($t = 150$ nm) of the NbTiN membranes permits their modeling as infinitely thick slabs. The Casimir pressure, $P(d, T)$, between two identical parallel slabs is given by the Lifshitz formula as (negative pressures indicate attraction):

$$P(d, T) = -\frac{k_B T}{\pi} \sum_{l=0}^{\infty} \int_0^{\infty} dk_{\perp} k_{\perp} q_l \sum_{\alpha} \left[\frac{e^{2dq_l}}{r_{\alpha}^2(i\xi_l, k_{\perp})} - 1 \right]^{-1}, \quad (\text{S.38})$$

where k_B represents the Boltzmann constant, k_{\perp} the in-plane momentum, the prime on the summation signifies that the $l = 0$ term is assigned a weight of one-half, $\xi_l = 2\pi l k_B T / \hbar$ are the imaginary Matsubara frequencies, $q_l = \sqrt{\xi_l^2 / c^2 + k_{\perp}^2}$, and the summation over $\alpha = \text{TE, TM}$ encompasses the independent polarization states of the electromagnetic field, namely transverse magnetic and transverse electric. The symbols $r_{\alpha}(i\xi_l, k_{\perp})$ denote the Fresnel reflection coefficients of the slab:

$$r_{\text{TE}}(i\xi_l, k_{\perp}) = \frac{q_l - s_l}{q_l + s_l}, \quad (\text{S.39})$$

$$r_{\text{TM}}(i\xi_l, k_\perp) = \frac{\epsilon_l q_l - s_l}{\epsilon_l q_l + s_l}, \quad (\text{S.40})$$

where $s_l = \sqrt{\epsilon_l \xi_l^2 / c^2 + k_\perp^2}$ and $\epsilon_l \equiv \epsilon(i\xi_l)$. To compute the frequency shift, we require the derivative $P'(d)$, which is given by Equation S.38 as:

$$P'(d, T) = 2 \frac{k_B T}{\pi} \sum_{l=0}^{\infty} \int_0^\infty dk_\perp k_\perp q_l^2 \sum_\alpha \frac{e^{2dq_l} r_\alpha^2(i\xi_l, k_\perp)}{[e^{2dq_l} - r_\alpha^2(i\xi_l, k_\perp)]^2}, \quad (\text{S.41})$$

In our computational model, core electron contributions to the NbTiN permittivity are disregarded, and only intraband transitions are taken into account. For temperatures exceeding T_C , these transitions are accurately modeled by a Drude dielectric function:

$$\epsilon(i\xi) = 1 + \frac{\Omega^2}{\xi(\xi + \gamma)} \quad (\text{S.42})$$

where Ω represents the plasma frequency for intraband transitions, and γ is the relaxation frequency. We have assumed the plasma frequency, Ω , to be temperature-independent, using its room-temperature value. The relaxation frequency, γ , on the other hand, varies with temperature, typically decreasing as temperature decreases. At cryogenic temperatures, γ approaches a constant residual value that depends on the specific sample. Following standard practice, we relate the residual relaxation frequency to the room-temperature value, γ_0 , using the formula $\gamma = \gamma_0/\text{RRR}$, where RRR is the residual resistance ratio. The following Drude parameters were used: $\Omega = 5.33$ eV/ \hbar and $\gamma_0 = 0.465$ meV/ \hbar . Moreover, we took $\text{RRR} = 1$. The permittivity of NbTiN in the superconducting state was calculated using the Mattis-Bardeen formula for the conductivity $\sigma_{\text{BCS}}(\omega)$ [105], known to accurately represent the optical response of BCS superconductors [106]. While the general Mattis-Bardeen formula depends on both frequency (ω) and wavevector (q), the q -dependence is negligible in the dirty limit ($\ell/\xi_0 \ll 1$), where $\ell = v_F/\gamma$ the dirty limit is well satisfied ($\ell/\xi_0 = 1.4 \times 10^{-2}$). This is confirmed by optical measurements of NbTiN films in the THz region, that are in excellent agreement with the local dirty-limit of the Mattis-Bardeen formula [107]. Analytic continuation to imaginary frequencies [108], gives:

$$\sigma_{\text{BCS}}(i\xi) = \frac{\Omega^2}{4\pi} \left[\frac{1}{(\xi + \gamma)} + \frac{g(\xi; T)}{\xi} \right], \quad (\text{S.43})$$

The first term is the Drude contribution, and the second is the BCS correction. The explicit expression of $g(\xi)$ and its properties are discussed in [14]. The permittivity of superconducting NbTiN is then given by:

$$\epsilon_{\text{BCS}}(i\xi) = 1 + \frac{4\pi}{\xi} \sigma_{\text{BCS}}(i\xi) = 1 + \frac{\Omega^2}{\xi} \left[\frac{1}{\xi + \gamma} + \frac{g(\xi; T)}{\xi} \right], \quad (\text{S.44})$$

where Ω is the plasma frequency for intraband transition, and γ is the relaxation frequency. For NbTiN we adapt the values used from [14, 17], i.e. $\Omega = 5.33$ eV/ \hbar and $\gamma = 0.465$ eV/ \hbar . The function $g(\xi; T)$ that describes the modification as a result of BCS theory, can be expressed as

$$g(\xi; T) = \Theta(T_C - T) \int_{-\infty}^{\infty} \frac{d\epsilon}{E} \tanh\left(\frac{E}{2k_B T}\right) \text{Re}[G_+(i\xi, \epsilon)] \quad (\text{S.45})$$

where T_C is the superconducting phase transition temperature, $E = \sqrt{\epsilon^2 + \Delta^2}$, $\Theta(x)$ is the Heaviside step function, i.e. $\Theta(x) = 1$ for $x > 0$, and $\Theta(x) = 0$ for $x \leq 0$, and

$$G_+(z, \epsilon) = \frac{\epsilon^2 Q_+(z, E) + [Q_+(z, E) + i\hbar\gamma] \cdot A_+(z, E)}{Q_+(z, E) \cdot \{\epsilon^2 - [Q_+(z, E) + i\hbar\gamma]^2\}}, \quad (\text{S.46})$$

where

$$Q_+(z, E) = \sqrt{(E + \hbar z)^2 - \Delta^2}, \quad (\text{S.47})$$

and

$$A_+(z, E) = E(E + \hbar z) + \Delta^2, \quad (\text{S.48})$$

here Δ is the temperature-dependent superconducting gap, which can be calculated from BCS theory:

$$\Delta = c_1 k_B T_C \sqrt{1 - \frac{T}{T_C}} \left(c_2 + c_3 \frac{T}{T_C} \right), \quad (\text{S.49})$$

and $c_1 = 1.764$, $c_2 = 0.9963$, and $c_3 = 0.7735$.

From data shown in Fig. S21 the effective Casimir pressure between NbTiN films at a separation of 190 nm, near T_C , can be expressed as

$$P_{\text{Cas}}(d) \Big|_{d=190\text{nm}} \approx \frac{-1.081 \times 10^{-24}}{d^{3.507}} [\text{Pa}], \quad (\text{S.50})$$

with the separation d measured in meters. With this expression of the Casimir pressure, we can use FEM simulation to estimate how much the external Casimir pressure/force is acting on the membrane. In order to do that, we scale the Casimir pressure acting on the membrane by a factor β close to unity, i.e. $P_{\text{sim}} = (1 + \beta) \cdot P_{\text{Cas}}(d)$ with $|\beta| < 0.001$, and found the linear conversion factors from the the frequency shift $\Delta\omega^2$ to variations in the Casimir force ΔF_{Cas} , the Casimir pressure ΔP_{Cas} , and membrane center static deflection Δz_{Cas} . The conversion factors are 1.986×10^{-17} N/Hz², 3.941×10^{-11} Pa/Hz², and 1.592×10^{-20} m/Hz², for force, pressure, and center deflection, respectively. From the simulation results, one can calculate that for the membrane suspends over 190 nm gap, the total Casimir force is around -2.028×10^{-7} N, and the total center deflection is around -141.6 pm, indicating that the level of parallelism achieved in our device is state-of-the-art.

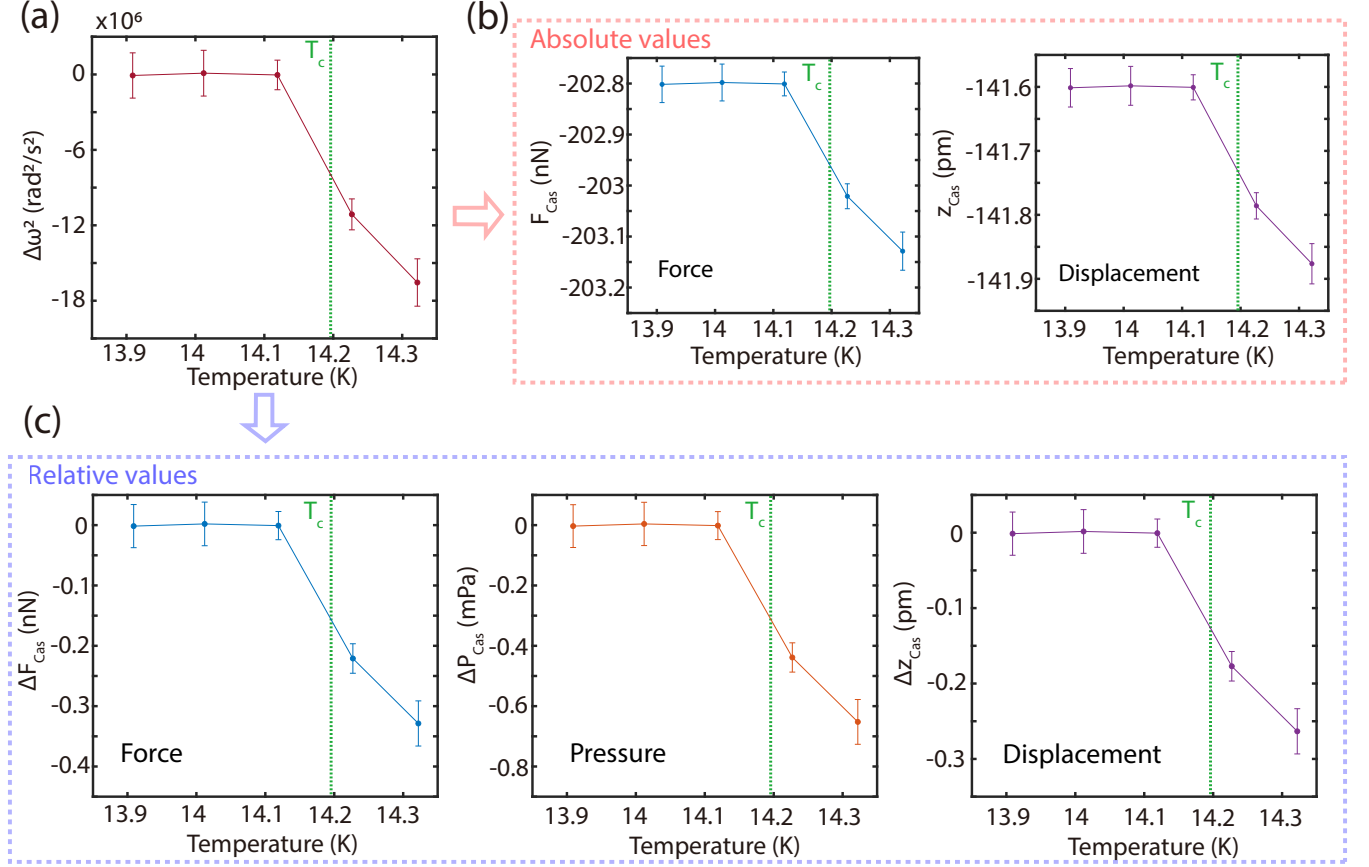


FIG. S22. Conversion of the shift of frequency square $\Delta\omega^2$ to parameters associated with the external Casimir force, using FEM simulation. (a) Experimentally measured shift of frequency square $\Delta\omega^2$ around T_C of small-gap membrane, after calibrating out the elastic force dependence on temperature. (b) Absolute values of the Casimir force variation and center deflection, corresponding to the value of $\Delta\omega^2$. (c) Relative values of the Casimir force, Casimir pressure, and static deflection of the center of the membrane, corresponding to the variation of the measured frequency square value $\Delta\omega^2$.

Supplementary Information H2: The $n = 0$ classical contribution: Drude vs plasma models

In this Section we study the $n = 0$ contribution to the Lifshitz formula S.38. This term represents a classical contribution to the Casimir pressure, which becomes the dominant contribution for separations $d \gg \lambda_T$, where $\lambda_T = \hbar c/k_B T$ is the thermal length. The precise form of this contribution has been a matter of significant controversy within the Casimir community for more than two decades, with experts divided between the Drude and plasma models. The Drude model accounts for electron scattering and dissipation, offering a more intuitive physical interpretation, while the plasma model, despite neglecting dissipation, aligns more closely with experimental observations. The key divergence lies in the treatment of the zero-frequency Matsubara term in the Lifshitz formula: the Drude approach predicts a vanishing transverse electric (TE) contribution, whereas the plasma model yields a finite term that significantly influences the force magnitude. This debate not only reflects discrepancies between theory and experiment but also challenges our fundamental understanding of the interplay between dissipation and quantum fluctuations.

The zero-frequency ($n = 0$) term in the discrete Matsubara frequency sum represents a static contribution to Lifshitz formulae Equations S.38 and S.41. It is well-established that this single term plays a dominant role in determining the temperature dependence of the Casimir pressure [112–114]. The $n = 0$ term can be separated into TM and TE polarization contributions:

$$P_{\text{cl}} \equiv P(d, T) \Big|_{n=0} = P_{\text{TM}}^{(0)} + P_{\text{TE}}^{(0)}, \quad (\text{S.51})$$

where

$$P_{\alpha}^{(0)} = -\frac{k_B T}{2\pi} \int_0^\infty dk_{\perp} k_{\perp}^2 \left[\frac{e^{2dk_{\perp}}}{r_{\alpha}^2(0, k_{\perp})} - 1 \right]^{-1}, \quad (\text{S.52})$$

where $\alpha = \text{TE}, \text{TM}$, and we set $r_{\alpha}^2(0, k_{\perp}) = \lim_{\xi \rightarrow 0} r_{\alpha}^2(i\xi, k_{\perp})$. The TM component $P_{\text{TM}}^{(0)}$ presents no difficulties; in the case of a conductor, $\lim_{\xi \rightarrow 0} \epsilon(i\xi) = \infty$, and it is easily demonstrated (see Eq. (S.40)) that $r_{\text{TM}}(0, k_{\perp}) = 1$. Evaluation of

Equation S.51 results into

$$P_{\text{TM}}^{(0)} = -\frac{k_B T}{2\pi d^3} \frac{\zeta(3)}{4}, \quad (\text{S.53})$$

where $\zeta(3) = 1.202$ is Riemann's zeta function. It is observed that the TM contribution exhibits universality, as its magnitude remains invariant across all conductors, irrespective of their superconducting or normal state. The TM contribution, by its nature, cannot induce a discontinuous jump in the Casimir pressure (or its gradient) at the superconducting transition, a feature that appears to be presented in our data.

The TE contribution $P_{\text{TE}}^{(0)}$, on the other hand, presents a considerably more intricate analysis. For normal (non-magnetic) conductors, the permittivity exhibits $1/\xi$ singularity as ξ approaches zero, according to Equation S.42. Consequently, one have $\lim_{\xi \rightarrow 0} s = \lim_{\xi \rightarrow 0} \sqrt{\epsilon(i\xi) \cdot \xi^2/c^2 + k_\perp^2} \approx k_\perp$, which implies that the TE reflection coefficient (Equation S.39) approaches zero as frequency vanishes:

$$r_{\text{TE}}(0, k_\perp) = 0, \quad (\text{Drude model approach}). \quad (\text{S.54})$$

The vanishing of r_{TE} means that the TE term does not contribute to the $n = 0$ term:

$$P_{\text{TE}}^{(0)} = 0, \quad (\text{Drude model approach}). \quad (\text{S.55})$$

Several room-temperature Casimir experiments[39, 40, 79, 81, 90] with metallic surfaces have shown discrepancies with theoretical predictions based on the Lifshitz formula. Surprisingly, it has been demonstrated that the aforementioned discrepancies are resolvable through the adoption of the following expression for the static TE reflection coefficient:

$$r_{\text{TE}}(0, k_\perp) = \frac{k_\perp - \sqrt{\Omega^2/c^2 + k_\perp^2}}{k_\perp + \sqrt{\Omega^2/c^2 + k_\perp^2}}, \quad (\text{plasma model approach}). \quad (\text{S.56})$$

Since the above formula for r_{TE} matches the $\xi \rightarrow 0$ limit of Equation S.39, when the plasma model is used for permittivity:

$$\epsilon(i\xi) = 1 + \frac{\Omega^2}{\xi^2}, \quad (\text{S.57})$$

the approach shown in Equation S.56, is known as the plasma-BCS approach. For a recent review of the problem of thermal Casimir effect and related experiments, see [115].

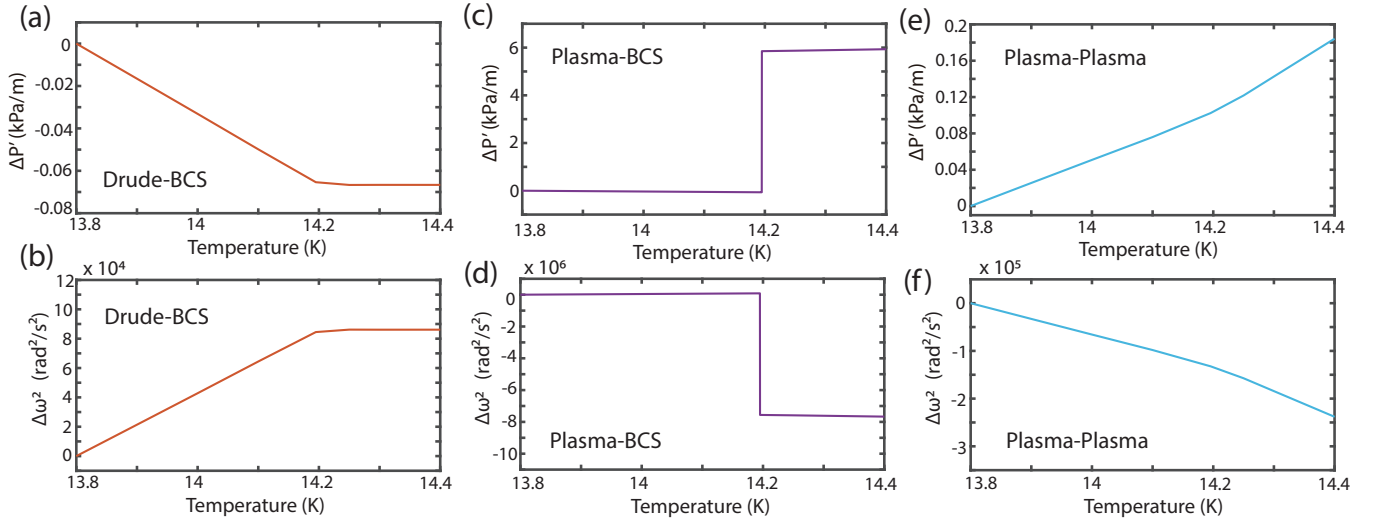


FIG. S23. Theoretical predictions for the Casimir pressure gradient variation $\Delta P'$ and the associated membrane frequency square shift $\Delta\omega^2$ across the superconducting transition. Panels (a) and (b) show curves computed using BCS model in the superconducting state ($T < T_C$) and the Drude model in the normal state ($T > T_C$). Panels (c) and (d) show curves computed using BCS model in the superconducting state ($T < T_C$) and the plasma model in the normal state ($T > T_C$). Panels (e) and (f) show curves computed using plasma model both in the superconducting state ($T < T_C$) and in the normal state ($T > T_C$).

The analysis thus far has concerned the normal state of our membrane ($T > T_c$). We now proceed to consider its superconducting state ($T < T_c$). In the superconducting state, the permittivity includes both a Drude component and a BCS component, as detailed in Equation S.44. The BCS contribution is proportional to the function $g(\xi; T)$, which, for small ξ , has the following expansion:

$$g(\xi; T) = \bar{\Omega}^2(T) + B(T) \cdot \xi \cdot \log\left(\frac{\Delta}{\hbar\xi}\right) + o(\xi), \quad (\text{S.58})$$

where $B(T) = (\sigma_0 \Delta(T)/2T) \cdot \text{sech}^2(\Delta(T)/2T)$, $\Delta(T)$ is the BCS gap, σ_0 is the dc conductivity in the normal state,

$$\bar{\Omega}^2(T) = \tilde{\omega}_s^2(T) \cdot \Omega^2. \quad (\text{S.59})$$

Here $\tilde{\omega}_s(T)$ represents the (normalized) effective superfluid plasma frequency [108]:

$$\tilde{\omega}_s(T) = \frac{\pi}{2\eta} \tanh\left(\frac{1}{4\eta \cdot t_{\text{red}}}\right) - \frac{1}{\eta^2} \int_0^\infty dx \frac{\tanh(E(x)/2t_{\text{red}})}{E(x)(4x^2 + 1)}, \quad (\text{S.60})$$

where $\eta = \hbar\gamma/2\Delta(T)$, $t_{\text{red}} = k_B T/\hbar\gamma$, and $E(x) = \sqrt{x^2 + 1/(4\eta^2)}$. It is noted that $0 < \tilde{\omega}_s(T) < 1$, implying $\bar{\Omega}(T) < \Omega$. Equations S.44 and S.58 show that ϵ_{BCS} exhibits a $1/\xi^2$ singularity as $\xi \rightarrow 0$, similar to the plasma model Equation S.57, which results in the following expression of the TE reflection coefficient of a BCS superconductor:

$$r_{\text{TE}}(0, k_\perp) = \frac{k_\perp - \sqrt{\bar{\Omega}(T)^2/c^2 + k_\perp^2}}{k_\perp + \sqrt{\bar{\Omega}(T)^2/c^2 + k_\perp^2}}, \quad (\text{BCS model for } T < T_c). \quad (\text{S.61})$$

TABLE S2. Alternative approaches for calculating the $n = 0$ contribution to the Casimir force.

Approach	Drude-BCS	Plasma-BCS	Plasma-Plasma
Temperature	$T > T_C$		
Model	Drude	Plasma	Plasma
$r_{\text{TM}}(0, k_\perp)$	$r_{\text{TM}} = 1$	$r_{\text{TM}} = 1$	$r_{\text{TM}} = 1$
$r_{\text{TE}}(0, k_\perp)$	$r_{\text{TE}} = 0$	$r_{\text{TE}} = \frac{k_\perp - \sqrt{\Omega^2/c^2 + k_\perp^2}}{k_\perp + \sqrt{\Omega^2/c^2 + k_\perp^2}}$	$r_{\text{TE}} = \frac{k_\perp - \sqrt{\Omega^2/c^2 + k_\perp^2}}{k_\perp + \sqrt{\Omega^2/c^2 + k_\perp^2}}$
Temperature	$T < T_C$		
Model	BCS	BCS	Plasma
$r_{\text{TM}}(0, k_\perp)$	$r_{\text{TM}} = 1$	$r_{\text{TM}} = 1$	$r_{\text{TM}} = 1$
$r_{\text{TE}}(0, k_\perp)$	$r_{\text{TE}} = \frac{k_\perp - \sqrt{\Omega^2/c^2 + k_\perp^2}}{k_\perp + \sqrt{\Omega^2/c^2 + k_\perp^2}}$	$r_{\text{TE}} = \frac{k_\perp - \sqrt{\Omega^2/c^2 + k_\perp^2}}{k_\perp + \sqrt{\Omega^2/c^2 + k_\perp^2}}$	$r_{\text{TE}} = \frac{k_\perp - \sqrt{\Omega^2/c^2 + k_\perp^2}}{k_\perp + \sqrt{\Omega^2/c^2 + k_\perp^2}}$

Supplementary Information H3: Three different approaches for the Casimir effect between superconductors

For our computations, we considered three different approaches to calculate the Casimir pressure. In all approaches, the positive Matsubara modes ($n > 0$) were computed using identical expressions for the permittivity of NbTiN: the Drude model Equation (S.42) for $T > T_c$, and the BCS formula Equation (S.44) for $T < T_c$. Additionally, for $n = 0$, we set $r_{\text{TM}}(0, k_\perp) = 1$ in all cases. The three approaches differ in the expressions used for the static TE reflection coefficient $r_{\text{TE}}(0, k_\perp)$, as summarized in Table (S2):

Drude-BCS approach: in this approach, $r_{\text{TE}}(0, k_\perp) = 0$ for $T > T_c$ (Equation (S.54)), and the BCS expression Equation (S.61) is used for $T < T_c$. As shown in panel (a) of Fig. (S23) this approach predicts a smooth decrease in the pressure gradient as the temperature increases through T_c , failing to explain the observed jump in $\Delta P'$.

Plasma-BCS approach: in this approach, for $T > T_c$ we use the plasma-model formula for $r_{\text{TE}}(0, k_\perp)$ (Equation (S.56)), and for $T < T_c$ the BCS expression Equation (S.61) is used. The plasma frequency $\Omega = 5.33 \text{ eV}/\hbar$ used corresponds to the optical response of NbTiN in the infrared region. As depicted in panel (c) of Fig. (S23) this approach does predict a jump in

$\Delta P'$, consistent with our experimental observations.

Plasma-Plasma approach: in this approach, the plasma-model formula for $r_{TE}(0, k_{\perp})$ (Equation (S.56)) is used both for $T > T_c$ and $T < T_c$. As shown in panel (e) of Fig. (S23) this approach predicts a smooth increase in the pressure gradient as the temperature increases through T_c , failing to explain the observed jump in $\Delta P'$.

Fig. S24(a) and (b) present the experimental data alongside theoretical predictions from the Drude-BCS and Plasma-BCS approaches for the variations in pressure gradient ($\Delta P'$) and membrane frequency shift $\Delta\omega^2$, respectively. The Drude-BCS approach is clearly inconsistent with the data, whereas the Plasma-BCS approach predicts jumps in $\Delta P'$ and $\Delta\omega^2$ that are approximately half the experimental values, suggesting its potential to explain the observed phenomena. It is noted that the Plasma-BCS approach can fully reproduce the experimental data with a plasma frequency of $\Omega = 12.7$ eV/h. As our current understanding of the plasma approach to the Casimir effect provides no strong justification for limiting Ω to the material's infrared optical response, the potential for employing a different value cannot be dismissed.

Our observation of a sudden resonance frequency shift during the membrane's superconducting transition, if attributable to the Casimir force, would be the first experimental evidence of the superconducting transition's influence on the Casimir effect. However, interpreting the data in this manner reveals two unexpected features. First, the sign of the frequency shift indicates a decrease in the Casimir pressure gradient during the transition, which contradicts the intuition that a superconducting surface, acting as a near-ideal mirror, should increase the Casimir force. Second, and perhaps more significantly, the abrupt frequency shift at the critical temperature seems to be inconsistent with the second-order nature of the superconducting transition. Since the Casimir force is the negative derivative of the Helmholtz free energy \mathcal{F} of the system with respect to separation [38], $F_{\text{Cas}} = -\partial\mathcal{F}/\partial d$, F_{Cas} is expected to be continuous across the transition. Furthermore, the smooth confluence of the BCS permittivity with the Drude permittivity at the superconducting transition temperature provides another reason to expect a continuous change in the Casimir force. The Drude-BCS theory of the Casimir effect in superconductors, as outlined in [14], cannot replicate the observed jump in the Casimir pressure, predicting instead a smooth increase in Casimir pressure. Conversely, the Plasma-BCS approach semi-quantitatively reproduces the observed behavior. The established agreement of the plasma approach with room-temperature Casimir experiments [39, 40, 79, 81, 90] suggests its expected applicability to the normal state of the membrane.

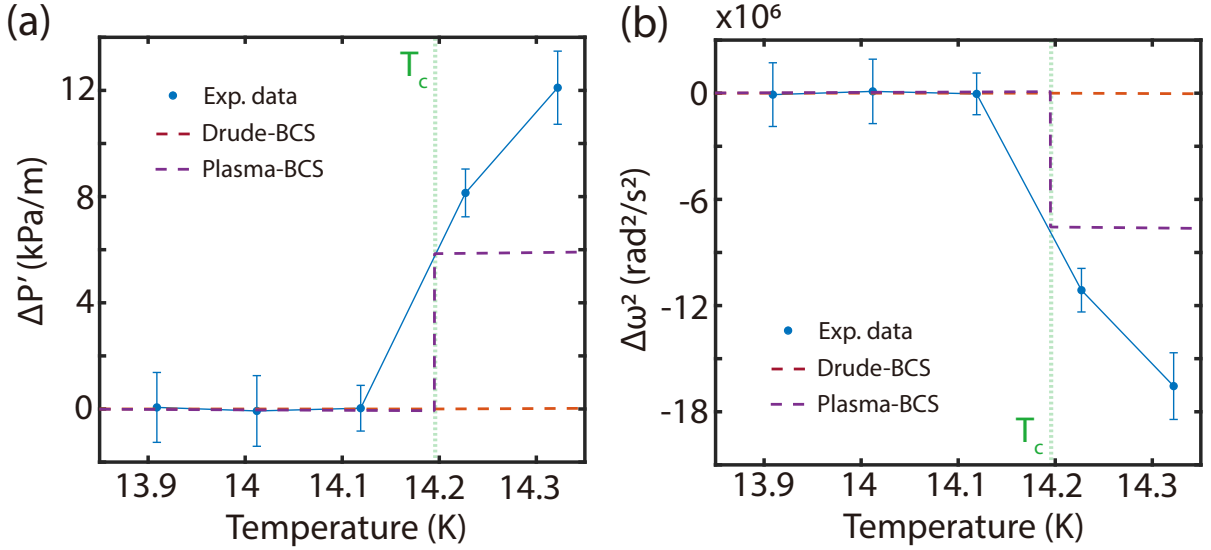


FIG. S24. Comparison of the experimental data and the theoretical analysis, on the abrupt changes in the (a) pressure gradient, and in the (b) membrane frequency square shift. The plasma-BCS approach seems capable of explaining the abrupt changes occurring at T_c .

SUPPLEMENTARY INFORMATION I: QUALITY FACTOR OF NANOMEMBRANES AS A FUNCTION OF TEMPERATURE

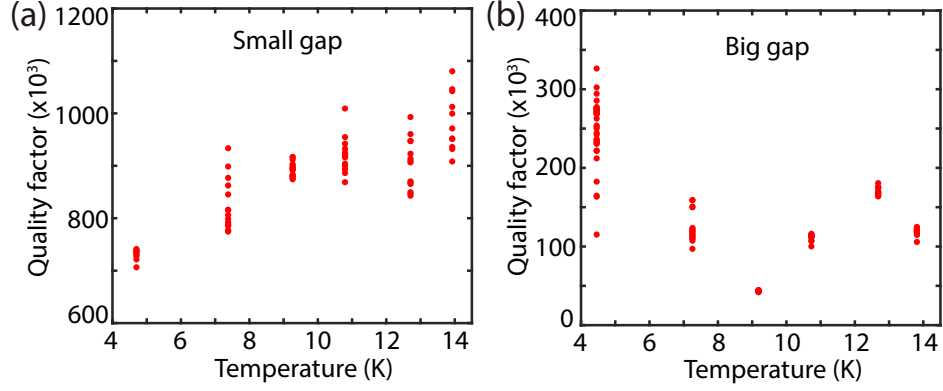


FIG. S25. Quality factor of $709 \times 709 \mu\text{m}^2$ nanomembranes over small- (Panel (a)) and big-gap (Panel (b)) Casimir cavities, as a function of temperature. The temperature range is from 4.45 K to 14 K. For both gap sizes, every temperature dataset has at least 10 data points.

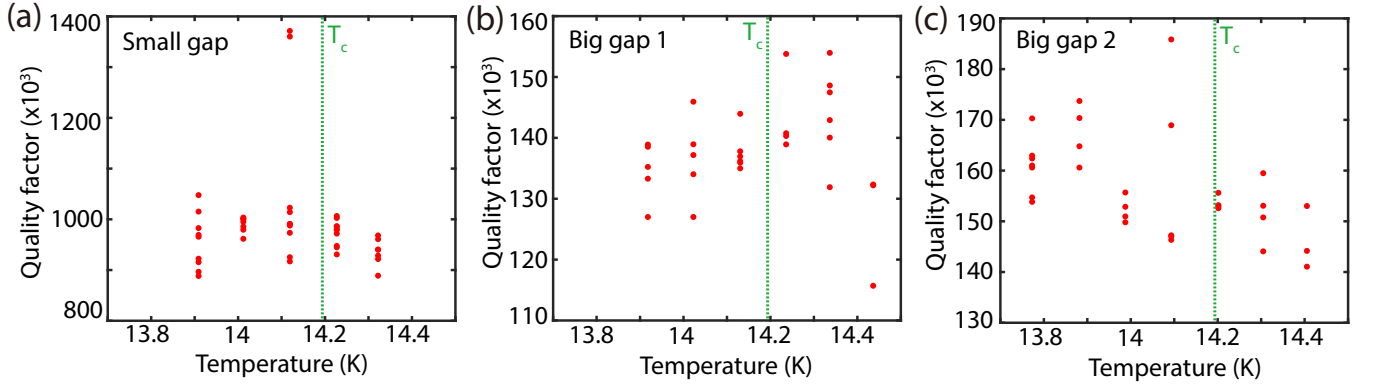


FIG. S26. Quality factor of $709 \times 709 \mu\text{m}^2$ nanomembranes over small- (Panel (a)) and big-gap (Panels (b) and (c)) Casimir cavities, as a function of temperature. The temperature range is near the superconducting phase transition temperature $T_c = 14.2$ K.

SUPPLEMENTARY INFORMATION J: LOGSCALE COMPARISON ON VARIOUS CASIMIR FORCE MEASUREMENTS

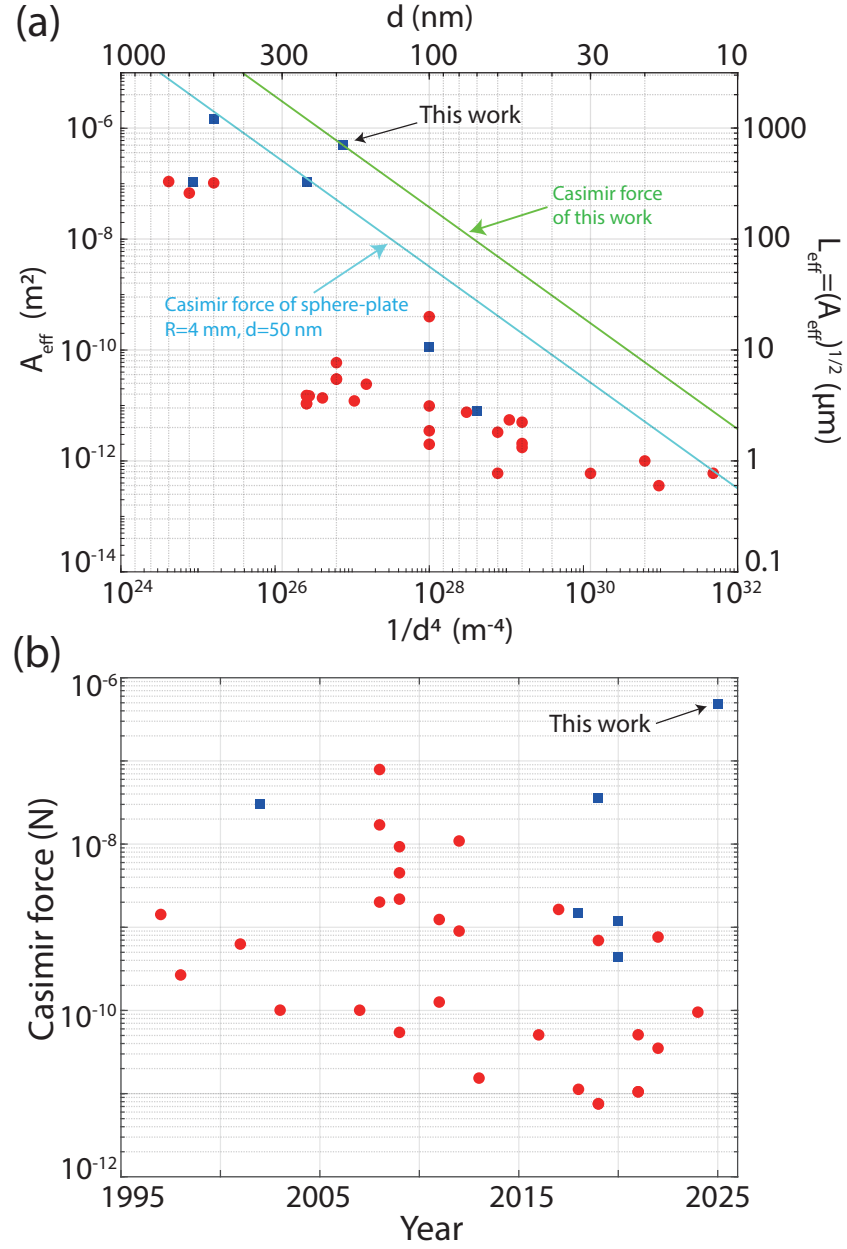


FIG. S27. Studies on Casimir effects. (a) The results are sorted out according to their minimum separation and effective areas. Data points further to the top right correspond a stronger Casimir force. (b) The results are sorted out according to their publication year, the vertical axis represents their corresponding Casimir force shown in log scale. The blue squares represent plate-plate experiments, and the red circles represent sphere-plate experiments.

TABLE S3. Casimir experiments with plate-plate configuration. (* radius of circular drum)

Ref	Size (μm)	Area (m^2)	Min Sep (nm)	Force (N)	Year
[6]	1200×1200	1.44×10^{-6}	500	2.99718×10^{-8}	2002
[16]	384×0.3	1.152×10^{-10}	100	1.49859×10^{-9}	2018
[7]	330×330	1.089×10^{-7}	250	3.62659×10^{-8}	2019
[23]	20×0.40	8.0×10^{-12}	70	4.3344×10^{-10}	2020
[32]	R=185 *	1.07518×10^{-7}	585	1.19423×10^{-9}	2020
This work	709×709	4.9×10^{-7}	190	4.89117×10^{-7}	2025
Average (except this work)				1.3873×10^{-8}	
Median (except this work)				1.4986×10^{-9}	

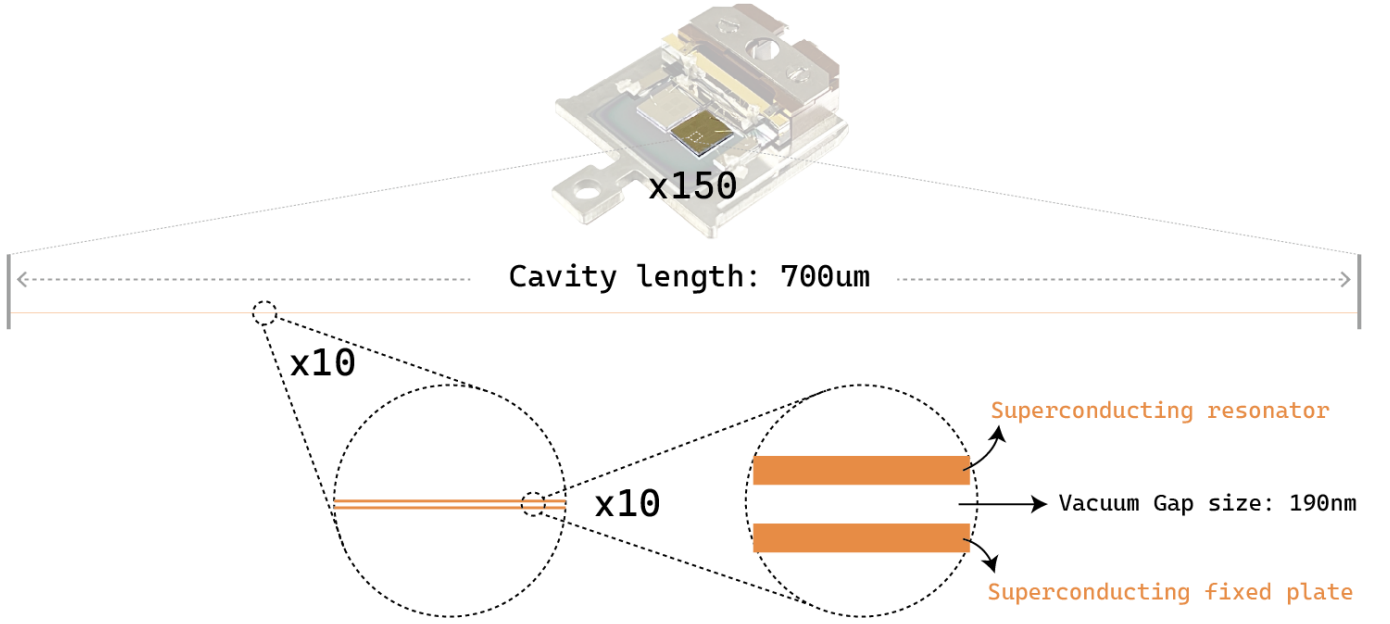


FIG. S28. Schematic of the Casimir cavity realized in this paper is presented at realistic scales. The scale drawing, representing the fabricated devices, exhibits extraordinary aspect ratios: a ratio of 4574 between its lateral dimensions and the resonator thickness, and a ratio of 3732 between its lateral dimensions and the vacuum gap.

TABLE S4. Casimir experiments with sphere-plate configuration. The effective area of the sphere-plate configuration is defined as $A_{\text{eff}} = R/d_{\text{min}}$, where R is the radius of the sphere, and d_{min} is the minimum separation. The ideal Casimir force calculated in this table is assuming the configurations are made of perfectly conducting plates, for a better comparison of their geometrical sizes, regardless of the materials.

Ref	Radius (um)	Effective Area (m ²)	Min Sep (nm)	Force (N)	Year
[2]	113000	6.78×10^{-8}	600	1.42528×10^{-9}	1997
[68]	98	9.8×10^{-12}	100	2.66995×10^{-10}	1998
[69]	100	7.57×10^{-12}	75.7	6.28042×10^{-10}	2001
[70]	296	5.92×10^{-11}	200	1.00804×10^{-10}	2003
[71]	151.3	2.4208×10^{-11}	160	1.00636×10^{-10}	2007
[35]	50	6.0×10^{-13}	12	7.8832×10^{-8}	2008
[72]	19.9	5.97×10^{-13}	30	2.00801×10^{-9}	2008
[62]	50	1.0×10^{-12}	20	1.70277×10^{-8}	2008
[73]	20	2.0×10^{-12}	100	5.44887×10^{-11}	2009
[74]	100	5.0×10^{-12}	50	2.17955×10^{-9}	2009
[75]	207000	1.035×10^{-7}	500	4.51167×10^{-9}	2009
[76]	19.9	3.582×10^{-13}	18	9.29634×10^{-9}	2009
[77]	10	6.0×10^{-13}	60	1.26131×10^{-10}	2011
[78]	156000	1.092×10^{-7}	700	1.2391×10^{-9}	2011
[40]	41.3	2.065×10^{-12}	50	9.00153×10^{-10}	2012
[11]	4000	4.0×10^{-10}	100	1.08977×10^{-8}	2012
[79]	61.7	1.36974×10^{-11}	222	1.53639×10^{-11}	2013
[81]	149.3	2.986×10^{-11}	200	5.08448×10^{-11}	2016
[17]	100	5.5×10^{-12}	55	1.63753×10^{-9}	2017
[83]	60.8	1.4896×10^{-11}	245	1.12637×10^{-11}	2018
[84]	43.446	1.08615×10^{-11}	250	7.57541×10^{-12}	2019
[85]	55	3.3×10^{-12}	60	6.93722×10^{-10}	2019
[86]	43	1.075×10^{-11}	250	7.49765×10^{-12}	2019
[87]	60.35	1.50875×10^{-11}	250	1.05229×10^{-11}	2021
[89]	60.35	1.50875×10^{-11}	250	1.05229×10^{-11}	2021
[90]	149.7	2.994×10^{-11}	200	5.0981×10^{-11}	2021
[91]	69.1	1.20925×10^{-11}	175	3.51269×10^{-11}	2022
[92]	35	1.75×10^{-12}	50	7.62842×10^{-10}	2022
[93]	35	3.5×10^{-12}	100	9.53552×10^{-11}	2024
Average				4.5856×10^{-9}	
Median				2.6700×10^{-10}	